

Title:

DATA TESTING OF ENDF/B-VI WITH MCNP: CRITICAL
EXPERIMENTS, THERMAL-REACTOR LATTICES, AND
TIME-OF-FLIGHT MEASUREMENTS

Author(s):

Russell D. Mosteller
Stephanie C. Frankle
Phillip G. Young

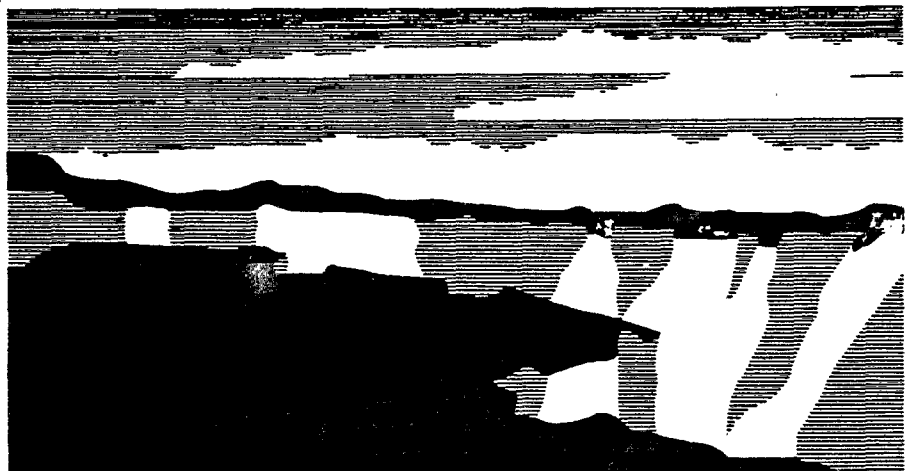
Submitted to:

Advances in Nuclear Science and Technology

Los Alamos

NATIONAL LABORATORY

Los Alamos National Laboratory, an affirmative action/equal opportunity employer, is operated by the University of California for the U.S. Department of Energy under contract W-7405-ENG-36. By acceptance of this article, the publisher recognizes that the U.S. Government retains a nonexclusive, royalty-free license to publish or reproduce the published form of this contribution, or to allow others to do so, for U.S. Government purposes. The Los Alamos National Laboratory requests that the publisher identify this article as work performed under the auspices of the U.S. Department of Energy. Los Alamos National Laboratory strongly supports academic freedom and a researcher's right to publish; therefore, the Laboratory as an institution does not endorse the viewpoint of a publication or guarantee its technical correctness.



**DATA TESTING OF ENDF/B-VI WITH MCNP:
CRITICAL EXPERIMENTS, THERMAL-REACTOR
LATTICES, AND TIME-OF-FLIGHT MEASUREMENTS**

Russell D. Mosteller,¹ Stephanie C. Frankle,²
and Phillip G. Young³

¹Technology and Safety Assessment Division

²Applied Theoretical and Computational Physics Division

³Theoretical Division

Los Alamos National Laboratory

Los Alamos, NM 87545

INTRODUCTION

The United States evaluated nuclear database, ENDF/B, is organized and implemented by the Cross Section Evaluation Working Group (CSEWG), which is a cooperative industrial/governmental activity involving, at its peak, some 20 different organizations. Since its inception in 1966, CSEWG systematically improved the evaluated database as new experimental and theoretical information became available, periodically issuing new versions of the ENDF/B library. The ENDF/B-VI file initially was issued in 1989-1990 and has been followed by three updated releases, with a fourth to follow soon. The purpose of this paper is to review the status of the ENDF/B-VI data file and to describe recent data testing results obtained with the Monte Carlo N-Particle (MCNP) code.¹

Deficiencies in ENDF/B-V

The previous version of the database is referred to as ENDF/B-V.2, which was originally issued² in 1979 but was followed by significant updating (Release 2)³ in 1981. Thorough reviews of the fission-reactor-related cross-section data in ENDF/B-V.2 were published⁴ in 1984. While Version V represented a significant improvement over previous versions, it was soon apparent that limitations in the formats made substantive improvement of the data at lower energies (resonance region) difficult and made adaptation of the file for higher energy applications (above 20 MeV) virtually impossible. Furthermore, at the time of issuance of ENDF/B-V, it was only possible to include neutron-induced data in the

official ENDF/B file, even though the need for evaluated charged-particle-induced data for fusion reactors and other applications was apparent. Finally, in the period following the issuance of ENDF/B-V.2, several important differential measurements were completed, and advances in nuclear theory and evaluation methods occurred that made updating of the database desirable. A number of deficiencies were identified in both content and breadth of coverage that provided further impetus for improving the database.

Objectives for ENDF/B-VI

Prior to ENDF/B-VI, the only resonance-parameter formalisms allowed were single-level Breit-Wigner,⁵ multi-level Breit Wigner,⁶ and Adler-Adler⁷ formalisms. With only these possibilities available and with the procedures in effect at that time, it was not possible to adequately represent the high-resolution data that were becoming available, particularly from the Oak Ridge Electron Linear Accelerator (ORELA). Additionally, many of the resolved resonance parameter evaluations only extended to relatively low incident neutron energy, well below the energy at which modern, high-resolution measurements were possible. For example, the ENDF/B-V.2 resolved resonance parameter evaluations for ²³⁵U and ²³⁹Pu only extend to 82 and 301 eV, respectively.

Beginning around 1985, there was increased interest in expanding evaluated data files to higher incident energies for both neutrons and charged particles, initially for national defense applications and later for accelerator-based transmutation technologies and accelerator-shielding applications. The most serious limitation in the ENDF/B format for higher energy evaluations was the inability to represent energy-angle correlated spectral distributions of emitted neutrons and charged particles. The formats at that time did permit a form of energy-angle correlations for emitted neutrons (only) to be given, but the method was cumbersome and inadequate. Most importantly, processing codes did not exist to handle this option, because it was generally felt that improvements to the format were needed before any processing-code development was merited.

Serious deficiencies in energy balance were noted in ENDF/B-V by MacFarlane,⁸ which led to questions as to the efficacy of the file for damage and kerma calculations. Some of the evaluations identified as having energy-conservation problems were quite important for either fusion or fission applications (or both), particularly for several important structural materials (Cr, ⁵⁵Mn, Fe, Ni). Additionally, many evaluations did not contain covariance information, and there were serious deficits in both the coverage and the scope of fission-product evaluations. Finally, the concept of simultaneous evaluations had not yet materialized, and, for example, evaluations of (n,γ) and (n,f) data for ²³⁵U and ²³⁹Pu were done independently. While data-testing results indicated that the quality of ENDF/B-V evaluations was high,⁹ it was still possible for small systematic shifts or biases to be present, and it was felt desirable to analyze simultaneously as many of the important reactions as possible.

Efforts to modernize and update the ENDF/B-V.2 file began in the mid-1980s. The primary objectives were to (1) modernize and generalize the ENDF/B format for wider scope and applicability, especially in the resonance region and for higher energy evaluations; (2) perform a state-of-the-art simultaneous evaluation of the standard cross-section reactions, including all other reactions with significant absolute cross-section databases and with ratio links to the standards; (3) correct the most serious energy-balance problems, particularly for structural materials, utilizing isotopic data evaluations; (4) significantly update fission-product yield and decay data files; (5) incorporate new high-resolution total, scattering, (n,γ), and (n,f) cross-section data in high-quality resonance parameter analyses; and (6) extend evaluations to higher energies and to include energy-angle correlated neutron and charged-particle emission data utilizing the new format developments.

Status of ENDF/B-VI Data File

Four separate distributions of ENDF/B-VI data files have occurred thus far, and a new distribution is in preparation. The initial distribution (Release 0) occurred in 1990, which included the extensively revised standards cross-section materials.^{10,11} This distribution was followed by a largely corrective Release 1 in 1991. Additional distributions occurred in 1993 (Release 2) and 1995 (Release 3), and a new distribution (Release 4) is planned for 1996. A summary of the major new ENDF/B-VI evaluations that have been released to date is given in Table 1. Not included in Table 1 are a number of substantive revisions of the evaluated data for key fission products, primarily in the resonance region. Summary documentation for Releases 1-3 is given in Ref. 12.

Standards Cross Sections. The methodology used in the simultaneous standards evaluation¹³ is especially important for fission-reactor applications because it permits inclusion of several important control and actinide materials in the analysis. In addition to data for the usual standards cross sections (which include the $^{10}\text{B}(\text{n},\alpha)$ and $^{235}\text{U}(\text{n},\text{f})$ reactions), absolute cross-section measurements and connecting ratio data for the $^{238}\text{U}(\text{n},\gamma)$, $^{238}\text{U}(\text{n},\text{f})$, and $^{239}\text{Pu}(\text{n},\text{f})$ reactions were incorporated in the simultaneous analysis. While this technique improves absolute cross sections, it is especially effective in determining relative cross sections and covariances, hopefully eliminating some of the bias that has been evident in the past between uranium and plutonium critical systems.

Light-Element Cross Sections. Significantly improved evaluations are included in ENDF/B-VI for several light elements. Most important are the ^6Li and ^{10}B evaluations, which include the important (n,α) standards cross sections. The basis for these evaluations (and for the ^{14}N and ^{16}O evaluations below the inelastic threshold) are coupled-channel R-matrix analyses that facilitate accurate analysis of comprehensive experimental databases and, at the same time, permit inclusion of very accurate charged-particle and neutron total cross-section data. Important new evaluations also are included for ^7Li , ^9Be , ^{11}B , and C. In the case of ^9Be , a complete new evaluation was performed with special emphasis on accurately specifying the energy-angle correlated neutron emission spectra from $(\text{n},2\text{n})$ reactions.¹⁰ The new ^{11}B evaluation is primarily based on improved experimental data, with the most significant improvement occurring in the neutron total cross section, which in ENDF/B-V.2 is in error by as much as 40%.

Structural Materials. Fe, Ni, and Cr are among the most important structural materials for fission reactors. Separate evaluations were performed for all stable isotopes of each of these elements. The evaluations are based on analyses of experimental data and extensive new theoretical studies in the MeV region.¹⁴ Additionally, new multichannel resonance parameter analyses were performed¹⁵ for ^{56}Fe and ^{58}Ni using high-resolution transmission, capture, and scattering data from ORELA. A similar analysis of transmission and capture also is included in the ^{60}Ni evaluation. Finally, substantially improved new evaluations of V, ^{55}Mn , Co, ^{63}Cu , ^{65}Cu , ^{206}Pb , ^{207}Pb , and ^{208}Pb are included in ENDF/B-VI.

Major Actinides. New evaluations of resolved resonance parameters¹⁶ using the Reich-Moore multilevel formalism¹⁷ are included in the ENDF/B-VI evaluations for ^{235}U , ^{238}U , ^{239}Pu , and ^{241}Pu . Each of these resonance-parameter evaluations covers a considerably larger energy range than does the previous version of ENDF/B and thereby reduces difficulties and uncertainties in calculating self-shielding effects. The ^{235}U resolved resonance region extends to 2.25 keV, ^{238}U to 10 keV, and ^{239}Pu to 1 keV. The simultaneous standards evaluation provides significantly improved (n,f) cross sections above neutron energies of ~ 10 keV for ^{235}U , ^{238}U , and ^{239}Pu , and improved (n,γ) cross sections in

Table 1. Major new neutron cross-section evaluations in ENDF/B-VI.

Material	Major Applications	Release Number	Responsible Laboratory ^a	Evaluators
¹ H	Standards, coolant	1	LANL	D. Dodder, G. Hale
² H	Coolant	3	LANL	P. Young, L. Stewart
³ He	Standards	1	LANL	G. Hale
⁶ Li	Standards, ³ H breeding	1	LANL	G. Hale, P. Young
⁷ Li	³ H breeding	0	LANL	P. Young, T. Beynon
⁹ Be	Shielding, neutron multiplication	0	LLNL	S. Perkins, E. Plechaty, R. Howerton
¹⁰ B	Standards, control	1	LANL	G. Hale, P. Young
¹¹ B	Shielding	0	LANL	P. Young
C	Standards, shielding	1	ORNL	C. Fu, E. Axton
¹⁴ N	Coolant	3	LANL	P. Young, G. Hale, M. Chadwick
¹⁵ N	Coolant	0	LANL	E. Arthur, P. Young, G. Hale
¹⁶ O	Coolant	0	LANL	G. Hale, M. Chadwick, P. Young, Z. Chen
¹⁹ F	Coolant	0	CNDC	Z. Zhao, C. Fu, D. Larson
²³ Na	Coolant	1	ORNL	D. Larson
²⁷ Al	Structure	3	LANL	P. Young
V	Structure	0	ANL	A. Smith, D. Smith, R. Howerton, <i>et al.</i>
⁵⁰ Cr	Structure	1	ORNL	D. Hetrick, C. Fu, D. Larson, K. Shibata
⁵² Cr	Structure	1	ORNL	D. Hetrick, C. Fu, D. Larson, K. Shibata
⁵³ Cr	Structure	1	ORNL	D. Hetrick, C. Fu, D. Larson, K. Shibata
⁵⁴ Cr	Structure	1	ORNL	D. Hetrick, C. Fu, D. Larson, K. Shibata
⁵⁵ Mn	Structure	0	JAERI	K. Shibata
⁵⁴ Fe	Structure	1	ORNL	C. Fu, C. Perey, D. Hetrick, <i>et al.</i>
⁵⁶ Fe	Structure	1	ORNL	C. Fu, C. Perey, D. Hetrick, <i>et al.</i>
⁵⁷ Fe	Structure	1	ORNL	C. Fu, C. Perey, D. Hetrick, <i>et al.</i>
⁵⁸ Fe	Structure	1	ORNL	C. Fu, C. Perey, D. Hetrick, <i>et al.</i>
Co	Structure	2	ANL	A. Smith, P. Guenther, R. Howerton, <i>et al.</i>
⁵⁸ Ni	Structure	1	ORNL	D. Hetrick, C. Perey, D. Larson, C. Fu, <i>et al.</i>
⁵⁹ Ni	Structure	0	ORNL	F. Mann
⁶⁰ Ni	Structure	1	ORNL	D. Hetrick, C. Perey, D. Larson, C. Fu, <i>et al.</i>
⁶¹ Ni	Structure	1	ORNL	D. Hetrick, C. Perey, D. Larson, C. Fu, <i>et al.</i>
⁶² Ni	Structure	1	ORNL	D. Hetrick, C. Perey, D. Larson, C. Fu, <i>et al.</i>
⁶⁴ Ni	Structure	1	ORNL	D. Hetrick, C. Perey, D. Larson, C. Fu, <i>et al.</i>

Table 1 (cont). Major new neutron cross-section evaluations in ENDF/B-VI.

Material	Major Applications	Release Number	Responsible Laboratory ^a	Evaluators
⁶³ Cu	Structure, conduction	2	ORNL	D. Hetrick, C. Fu, D. Larson
⁶⁵ Cu	Structure, conduction	2	ORNL	D. Hetrick, C. Fu, D. Larson
⁷³ Ge	Detector	2	WHC	R. Schenter, F. Schmittroth
⁸⁹ Y	Fission product	0	ANL	A. Smith, D. Smith, R. Howerton, <i>et al.</i>
⁹³ Nb	Activation, dose	1	ANL	A. Smith, D. Smith, R. Howerton
In	Control	0	ANL	A. Smith, D. Smith, P. Guenther
¹¹⁵ In	Control	0	WHC	F. Schmittroth, D. Smith, S. Chiba
¹⁵¹ Eu	Activation, dose	0	LANL	P. Young, E. Arthur
¹⁵³ Eu	Activation, dose	0	LANL	P. Young, E. Arthur
¹⁶⁵ Ho	Dose	0	LANL	P. Young, E. Arthur
¹⁸⁵ Re	Structure	0	ORNL	L. Weston, P. Young
¹⁸⁷ Re	Structure	0	ORNL	L. Weston, P. Young
¹⁹⁷ Au	Standards, dose	1	LANL	P. Young, E. Arthur
²⁰⁹ Pb	Shielding, neutron multiplication	0	ORNL	C. Fu, N. Larson, D. Larson
²⁰⁷ Pb	Shielding, neutron multiplication	0	ORNL	C. Fu, N. Larson, D. Larson
²⁰⁸ Pb	Shielding, neutron multiplication	0	ORNL	C. Fu, N. Larson, D. Larson
²⁰⁹ Bi	Shielding	0	ANL	A. Smith, D. Smith, P. Guenther
²³⁵ U	Fuel cycle	3	ORNL	L. Weston, P. Young, W. Poenitz, <i>et al.</i>
²³⁶ U	Fuel cycle	0	WHC	F. Mann, R. Schenter
²³⁸ U	Fuel cycle	2	ANL	A. Smith, W. Poenitz, M. Sowerby, <i>et al.</i>
²³⁷ Np	Fuel cycle	1	LANL	P. Young, E. Arthur, F. Mann
²³⁹ Np	Fuel cycle	0	ORNL	R. Wright, Y. Kanda
²³⁹ Pu	Fuel cycle	2	LANL	P. Young, L. Weston, H. Derrien, <i>et al.</i>
²⁴⁰ Pu	Fuel cycle	2	ORNL	L. Weston, E. Arthur
²⁴¹ Pu	Fuel cycle	3	ORNL	L. Weston, H. Derrien, <i>et al.</i>
²⁴¹ Am	Fuel cycle	3	LANL	P. Young, D. Madland
²⁴³ Am	Fuel cycle	0	ORNL	L. Weston
²⁴⁹ Bk	Fuel cycle	0	CNDC	D. Zhou, <i>et al.</i>
²⁴⁹ Cf	Fuel cycle	0	CNDC	D. Zhou, <i>et al.</i>

^a ANL = Argonne National Laboratory
 JAERI = Japan Atomic Energy Research Institute
 LLNL = Lawrence Livermore National Laboratory
 WHC = Westinghouse Hanford Company

CNDC = Chinese (Beijing) Nuclear Data Center
 LANL = Los Alamos National Laboratory
 ORNL = Oak Ridge National Laboratory

the same range for ^{238}U . Additionally, the new or updated theoretical analyses of the elastic scattering, (n,n') , $(n,2n)$, and $(n,3n)$ reactions for the major actinides provide significantly improved data for outgoing neutron cross sections, angular distributions, and emission spectra.

Yield, Decay, and Delayed-Neutron Data. Substantially expanded fission-product yield data files are provided in Version VI of ENDF/B. New or updated evaluations of independent, cumulative, and mass chain yields with uncertainties are given for 36 fissioning nuclides at one or more incident neutron energies.¹⁸ Evaluated yields for spontaneously fissioning nuclides also are included, so that a total of 60 nuclide-energy combinations is available, resulting in the formation of approximately 1100 different fission products. Decay data (average decay energies, decay spectra, and, to a lesser extent, cross sections) for many of the present 979 fission-product and actinide nuclides were improved for Version VI using new experimental measurements and nuclear-model calculations.¹⁹ Finally, delayed-neutron data are vastly improved in ENDF/B-VI as compared to ENDF/B-V.2. In particular, individual decay spectra and emission probabilities are included for some 271 delayed-neutron precursors, with temporal 6-group data provided for most of the fissionable nuclides.

Overview of MCNP

Development of Monte Carlo methods began at Los Alamos Scientific Laboratory, later renamed Los Alamos National Laboratory (LANL), during World War II. MCNP is the product of more than 50 years of research and more than 400 person-years of development.

Code Capabilities. MCNP is a general-purpose Monte Carlo code that can be used to perform a variety of types of calculations involving neutrons, photons, and/or electrons in one-, two-, and three-dimensional geometries. For the studies discussed herein, however, it was used only to calculate eigenvalues, neutron reaction rates, and fluxes.

MCNP employs three different types of estimators for k_{eff} : collision, absorption, and track-length. It then combines those estimators to produce k_{eff} in such a way that the associated standard deviation is minimized. All of the values reported herein for k_{eff} are based on the combined collision/absorption/track-length estimator.

Continuous-Energy Libraries. One of the principal advantages of MCNP is its ability to work with continuous-energy neutron libraries. A group-wise library requires preprocessing on a case-by-case basis to incorporate the effects of self-shielding, group-to-group scattering, and/or geometry (viz., Dancoff factors). A continuous-energy library, in contrast, eliminates the need for such preprocessing and all associated approximations. Continuous-energy MCNP libraries derived from ENDF/B-V and ENDF/B-VI specifications are available for a large number of isotopes and for some naturally occurring elements.²⁰

The ENDF/B-VI isotopic libraries are current through ENDF/B-VI Release 2 (ENDF/B-VI.2). In addition, a library based on the evaluation for ^{235}U in ENDF/B-VI Release 3 (ENDF/B-VI.3) has been generated for internal use at LANL, and calculations with that library are compared with results from ENDF/B-V and ENDF/B-VI.2 later in this paper. All of the libraries employed in this study are based on a temperature of 300 K.

The ENDF/B-V.2 and ENDF/B-VI.2 isotopic libraries for MCNP hereafter will be designated simply as the ENDF/B-V and ENDF/B-VI libraries unless otherwise noted.

DATA TESTING: CRITICAL EXPERIMENTS

Data testing has been performed for a large number of critical experiments. Those experiments have been selected to encompass most combinations of materials that are of interest in criticality safety. Where feasible, similar experiments have been included to ensure that the results are not distorted by some unique feature of a single experiment. In addition, in many cases more than one experiment from a particular set of experiments has been included so that the effect of variations within such a system can be evaluated.

Specifications for all of the experiments discussed herein have been approved either by the CSEWG or by the working group for the International Criticality Safety Benchmark Evaluation Project (ICSBEP). The detailed specifications for the CSEWG benchmarks are given in their benchmark-specifications report,²¹ while the ICSBEP specifications are given in the International Handbook of Evaluated Criticality Safety Benchmark Experiments.²² (In some cases, the specifications were approved subsequent to the last formal publication of those documents and therefore have not yet appeared in them.) Specifications for several of the experiments are given in both documents, and in such cases the ICSBEP specifications usually have been chosen. In most of those cases, the differences in the specifications are minor. However, the ICSBEP specifications provide an uncertainty for the benchmark value of k_{eff} , whereas the CSEWG specifications usually do not. The specific CSEWG and ICSBEP identifiers for each benchmark are given in Appendix A.

Except as noted, all of the MCNP calculations for these critical experiments utilized 440 generations of neutrons with 2500 neutrons per generation, and the first 40 generations were excluded from the statistics. Consequently, the quoted results are based on 1,000,000 active neutron histories.

Uranium Critical Experiments

The uranium critical experiments that have been used for data testing are summarized in Table 2. They include highly enriched uranium (HEU) and ^{233}U metal systems, low-enriched uranium (LEU) lattices, and HEU, LEU, and ^{233}U solutions. Fast neutrons produce most of the fissions in the metal systems, while thermal neutrons produce most of the fissions in the lattices and the solutions.

The benchmark values for k_{eff} for most of these experiments are unity, but some of them are slightly higher or slightly lower. There are two reasons for such differences. First, some of the benchmark specifications include idealizations that were made to simplify the representation of the experiment, and the benchmark k_{eff} was adjusted to account for the reactivity effect of those idealizations. Second, the configuration of some of the experiments was slightly supercritical when the measurement was made.

Metal Systems. The metallic uranium systems include experiments with HEU and with ^{233}U . The experiments with HEU include a bare sphere, two spheres that were reflected with normal uranium, two stacks of alternating platters of HEU and normal uranium, and a sphere and a cube of HEU that were reflected by water. The experiments with ^{233}U include a bare sphere and a sphere reflected by normal uranium. All of these experiments were performed at LANL, mostly during the 1950s.

Godiva^{23,24} is a bare sphere of HEU enriched to 93.71 wt.% in ^{235}U . It has a radius of 8.7407 cm and a density of 18.74 g/cm³.

Both the Topsy²⁵ and the FLATTOP-25^{23,26} configurations contain a sphere of HEU enclosed in a sphere of normal uranium. The inner Topsy sphere is slightly smaller and slightly less dense than the inner FLATTOP-25 sphere, but its enrichment is slightly higher. The Topsy reflector is slightly less dense than its FLATTOP-25 counterpart, but it is thicker. A summary of the specifications for the two configurations is given in Table 3.

Table 3. Specifications for the Topsy sphere and for FLATTOP-25.

Parameter	Topsy sphere		FLATTOP-25	
	Inner sphere	Outer sphere	Inner sphere	Outer sphere
Radius (cm)	6.0509	26.3709	6.1156	24.1242
Enrichment (wt.%)	93.5	0.711	93.2	0.711
Density (g/cm ³)	18.75	18.90	18.62	19.00

The two Jemima experiments²⁷ have circular disks of HEU and normal uranium stacked to form a cylinder. The cylinder of disks is supported by a steel platform. The Jemima pairs experiment alternates disks of HEU and normal uranium, while the triplets experiment has two disks of normal uranium between successive disks of HEU. In the ICSBEP idealizations of the Jemima experiments, all of the disks have an outer radius of 13.335 cm. The thicknesses of the idealized disks of HEU and normal uranium are 0.804 cm and 0.604 cm, respectively. The average enrichment of the HEU disks is 93.4 wt.% for the pairs experiment and 93.5 wt.% for the triplets experiment, while their average density is 18.73 g/cm³ for the pairs experiment and 18.74 g/cm³ for the triplets experiment. The average density for the disks of normal uranium is 18.99 g/cm³ for both experiments. The stack of idealized disks is 15.648 cm high for the pairs experiment and 24.973 cm high for the triplets experiment.

Both the water-reflected sphere^{28,29} and the water-reflected cube³⁰ of HEU are enclosed in a neutronically infinite medium of water. The sphere is more highly enriched than the cube (97.7 wt.% versus 94.0 wt.%), and it is very slightly more dense (18.79 g/cm³ versus 18.72 g/cm³). Consequently, the difference between the critical mass of the sphere (22.16 kg) and that of the cube (24.00 kg) is slightly larger than it would be because of just the difference in shape. The radius of the sphere is 6.5537 cm, and each side of the cube is 10.863 cm long. Most of the fissions for both of these cases are caused by fast neutrons, but the water sufficiently thermalizes enough neutrons that approximately 15% of the fissions are caused by thermal neutrons.

Jezebel-233²³ is a bare sphere of uranium enriched to 98.1 wt.% in ²³³U. It has a radius of 5.9838 cm and a density of 18.42 g/cm³.

FLATTOP-23^{23,26} is similar to FLATTOP-25 except that the inner sphere is enriched in ²³³U rather than ²³⁵U. The inner sphere has the same density and ²³³U enrichment as Jezebel-233, but its radius is 4.2058 cm. The outer sphere of normal uranium has a density of 19.00 g/cm³ and an outer radius of 24.1194 cm.

The results of the MCNP calculations for the metallic uranium benchmarks are summarized in Table 4.

For most of these cases, ENDF/B-V and ENDF/B-VI produce good agreement with the benchmark values of k_{eff} . However, the ENDF/B-VI results are in significantly better agreement with the benchmark k_{eff} for the two Jemima cases than are the corresponding ENDF/B-V results. Furthermore, with the exception of the water-reflected cases, the ENDF/B-VI result is consistently lower than the corresponding ENDF/B-V result. (The ENDF/B-VI sample means are lower than the corresponding ENDF/B-V sample means for the water-reflected cases too, but the difference is not statistically significant.)

Both ENDF/B-V and ENDF/B-VI slightly underpredict the benchmark k_{eff} for Godiva, although the ENDF/B-VI difference is about twice as large as the ENDF/B-V difference. Both libraries predict values of k_{eff} for the Topsy sphere and FLATTOP-25 that are within

Table 3. Specifications for the Topsy sphere and for FLATTOP-25.

Parameter	Topsy sphere		FLATTOP-25	
	Inner sphere	Outer sphere	Inner sphere	Outer sphere
Radius (cm)	6.0509	26.3709	6.1156	24.1242
Enrichment (wt.%)	93.5	0.711	93.2	0.711
Density (g/cm ³)	18.75	18.90	18.62	19.00

The two Jemima experiments²⁷ have circular disks of HEU and normal uranium stacked to form a cylinder. The cylinder of disks is supported by a steel platform. The Jemima pairs experiment alternates disks of HEU and normal uranium, while the triplets experiment has two disks of normal uranium between successive disks of HEU. In the ICSBEP idealizations of the Jemima experiments, all of the disks have an outer radius of 13.335 cm. The thicknesses of the idealized disks of HEU and normal uranium are 0.804 cm and 0.604 cm, respectively. The average enrichment of the HEU disks is 93.4 wt.% for the pairs experiment and 93.5 wt.% for the triplets experiment, while their average density is 18.73 g/cm³ for the pairs experiment and 18.74 g/cm³ for the triplets experiment. The average density for the disks of normal uranium is 18.99 g/cm³ for both experiments. The stack of idealized disks is 15.648 cm high for the pairs experiment and 24.973 cm high for the triplets experiment.

Both the water-reflected sphere^{28,29} and the water-reflected cube³⁰ of HEU are enclosed in a neutronically infinite medium of water. The sphere is more highly enriched than the cube (97.7 wt.% versus 94.0 wt.%), and it is very slightly more dense (18.79 g/cm³ versus 18.72 g/cm³). Consequently, the difference between the critical mass of the sphere (22.16 kg) and that of the cube (24.00 kg) is slightly larger than it would be because of just the difference in shape. The radius of the sphere is 6.5537 cm, and each side of the cube is 10.863 cm long. Most of the fissions for both of these cases are caused by fast neutrons, but the water sufficiently thermalizes enough neutrons that approximately 15% of the fissions are caused by thermal neutrons.

Jezebel-233²² is a bare sphere of uranium enriched to 98.1 wt.% in ²³³U. It has a radius of 5.9838 cm and a density of 18.42 g/cm³.

FLATTOP-23^{22,25} is similar to FLATTOP-25 except that the inner sphere is enriched in ²³³U rather than ²³⁵U. The inner sphere has the same density and ²³³U enrichment as Jezebel-233, but its radius is 4.2058 cm. The outer sphere of normal uranium has a density of 19.00 g/cm³ and an outer radius of 24.1194 cm.

The results of the MCNP calculations for the metallic uranium benchmarks are summarized in Table 4.

For most of these cases, ENDF/B-V and ENDF/B-VI produce good agreement with the benchmark values of k_{eff} . However, the ENDF/B-VI results are in significantly better agreement with the benchmark k_{eff} for the two Jemima cases than are the corresponding ENDF/B-V results. Furthermore, with the exception of the water-reflected cases, the ENDF/B-VI result is consistently lower than the corresponding ENDF/B-V result. (The ENDF/B-VI sample means are lower than the corresponding ENDF/B-V sample means for the water-reflected cases too, but the difference is not statistically significant.)

Both ENDF/B-V and ENDF/B-VI slightly underpredict the benchmark k_{eff} for Godiva, although the ENDF/B-VI difference is about twice as large as the ENDF/B-V difference. Both libraries predict values of k_{eff} for the Topsy sphere and FLATTOP-25 that are within

Table 4. Results for uranium metal systems.

Case title	Principal Fuel	Benchmark k_{eff}	k_{eff}		Δk	
			ENDF/B-V	ENDF/B-VI	ENDF/B-V	ENDF/B-VI
Godiva	HEU	1.0000 ± 0.0010	0.9983 ± 0.0006	0.9967 ± 0.0006	-0.0017 ± 0.0012	-0.0033 ± 0.0012
Topsy sphere	HEU	1.0000 ± 0.0030	1.0027 ± 0.0006	1.0013 ± 0.0006	0.0027 ± 0.0031	0.0013 ± 0.0031
FLATTOP-25	HEU	1.0000 ± 0.0030	1.0025 ± 0.0007	1.0010 ± 0.0006	0.0025 ± 0.0031	0.0010 ± 0.0031
Jemima pairs	HEU	0.9988 ± 0.0009	1.0025 ± 0.0006	0.9982 ± 0.0006	0.0037 ± 0.0011	-0.0006 ± 0.0011
Jemima triplets	HEU	0.9987 ± 0.0009	1.0053 ± 0.0006	0.9990 ± 0.0006	0.0066 ± 0.0011	0.0003 ± 0.0011
HEU sphere in water	HEU	0.9985 ± 0.0000	0.9965 ± 0.0008	0.9961 ± 0.0008	-0.0020 ± 0.0008	-0.0024 ± 0.0008
HEU cube in water	HEU	1.0000 ± 0.0010	1.0034 ± 0.0008	1.0026 ± 0.0008	0.0034 ± 0.0013	0.0026 ± 0.0013
Jezebel-233	^{235}U	1.0000 ± 0.0010	0.9932 ± 0.0006	0.9925 ± 0.0006	-0.0068 ± 0.0012	-0.0075 ± 0.0012
FLATTOP-23	^{235}U	1.0000 ± 0.0030	0.9993 ± 0.0007	1.0010 ± 0.0007	-0.0007 ± 0.0031	0.0010 ± 0.0031

a single standard deviation of the corresponding benchmark value. This behavior produces a significant swing between the values of k_{eff} for the bare Godiva sphere and the reflected spheres (approximately $0.0045 \Delta k$ for both ENDF/B-V and ENDF/B-VI). Neutron leakage from Godiva is nearly 60%, whereas the leakage from the reflected cases is only about 30%. A possible explanation is that both libraries tend to overpredict neutron leakage for high-leakage configurations.

Although the neutron leakage for both Jemima cases exceeds 50%, ENDF/B-VI produces values of k_{eff} for both cases that are in excellent agreement with the benchmark values. In contrast, ENDF/B-V produces a significant overestimate for k_{eff} for both cases. Sensitivity studies indicate that the better agreement for the ENDF/B-VI case is due primarily to changes in the fast cross sections for ^{235}U and, to a lesser extent, steel. The changes to the ^{238}U cross sections appear to have little or no impact on reactivity.

The two libraries produce results for the water-reflected cases that are statistically indistinguishable. Both libraries underpredict k_{eff} for the water-reflected sphere by approximately $0.0020 \Delta k$, and they both overpredict k_{eff} for the water-reflected cube by about the same amount. Consequently, on average, they produce very good agreement with the benchmarks for these two cases.

ENDF/B-V and ENDF/B-VI produce very similar results for Jezebel-233 and FLATTOP-23. This behavior is not surprising, because the differences between the ENDF/B-V and ENDF/B-VI evaluations for ^{233}U are very minor.

The same pattern that was observed for Godiva and FLATTOP-25 persists for Jezebel-233 and FLATTOP-23, although it is more exaggerated. The predicted value for k_{eff} for the bare sphere is low relative to the benchmark value, but the predicted value for the reflected configuration is in excellent agreement with the benchmark k_{eff} . Specifically, the reactivity swing between the bare and reflected configurations is approximately $0.006 \Delta k$ for ENDF/B-V and approximately 0.0085 for ENDF/B-VI. The pattern of neutron leakage also is similar: neutron leakage is slightly more than 60% for Jezebel-233, while it is approximately 30% for FLATTOP-23. The low values for Jezebel-233 strongly suggest that the fast cross sections for ^{233}U need to be improved.

In general, both the ENDF/B-V and the ENDF/B-VI libraries produce good agreement with metallic uranium benchmarks. The notable exceptions are Jezebel-233 and, for ENDF/B-V, the two Jemima cases. As noted previously, there are only very slight differences between the ENDF/B-V and ENDF/B-VI evaluations for ^{233}U , and so the two results for that case would be expected to be very similar. ENDF/B-V not only overestimates k_{eff} for the two Jemima cases, but it overestimates it by a significantly larger margin for the triplets case than for the pairs case. In marked contrast, ENDF/B-VI matches the benchmark k_{eff} very well, and the ENDF/B-VI values for the two cases are statistically indistinguishable.

Two additional patterns can be observed for these cases. First, ENDF/B-VI tends to produce lower values of k_{eff} for these cases than ENDF/B-V does, although the differences usually are small. Second, both libraries tend to underestimate k_{eff} for bare spheres of fissile material, but they both predict k_{eff} very accurately for reflected systems. This behavior may be due to leakage-related spectral effects. The neutron leakage for Godiva and Jezebel-233 is approximately 60%, but the leakage for the corresponding cases reflected by normal uranium is only about 30%.

Lattices. The three lattices of UO_2 fuel pins are based on experiments³¹ that were performed at Babcock & Wilcox's Lynchburg Research Center in 1970 and 1971. This series of experiments was designated as Core XI, and the individual experiments were characterized as different "loadings." The entire series of 17 experiments appears as ICSBEP benchmarks, and the 3 loadings that are discussed herein also have been accepted

as benchmarks by the ad hoc committee on reactor physics benchmarks,²² which is part of the Reactor Physics Division of the American Nuclear Society.

The experiments were performed inside a large aluminum tank that contained borated water and thousands of fuel pins. The water height for each loading was exactly 145 cm, and the soluble boron concentration in the water was adjusted until the configuration was slightly supercritical, corresponding to $k_{eff} = 1.0007$. The standard deviation in the measured soluble boron concentration is ± 3 parts per million (PPM), by weight.

For the three cases of interest, the central region of the configuration closely resembles a 3×3 array of pressurized-water-reactor (PWR) fuel assemblies. Each of these assemblies contains 225 lattice locations (i.e., in PWR parlance, they are "15 x 15" assemblies.) The 9 assemblies are surrounded by a buffer of fuel pins, and the buffer in turn is surrounded by a water reflector region. The buffer contains 2,936 pins for each of these cases, and the core as a whole contains more than 4,800 pins. A schematic of this arrangement is shown in Figure 1.

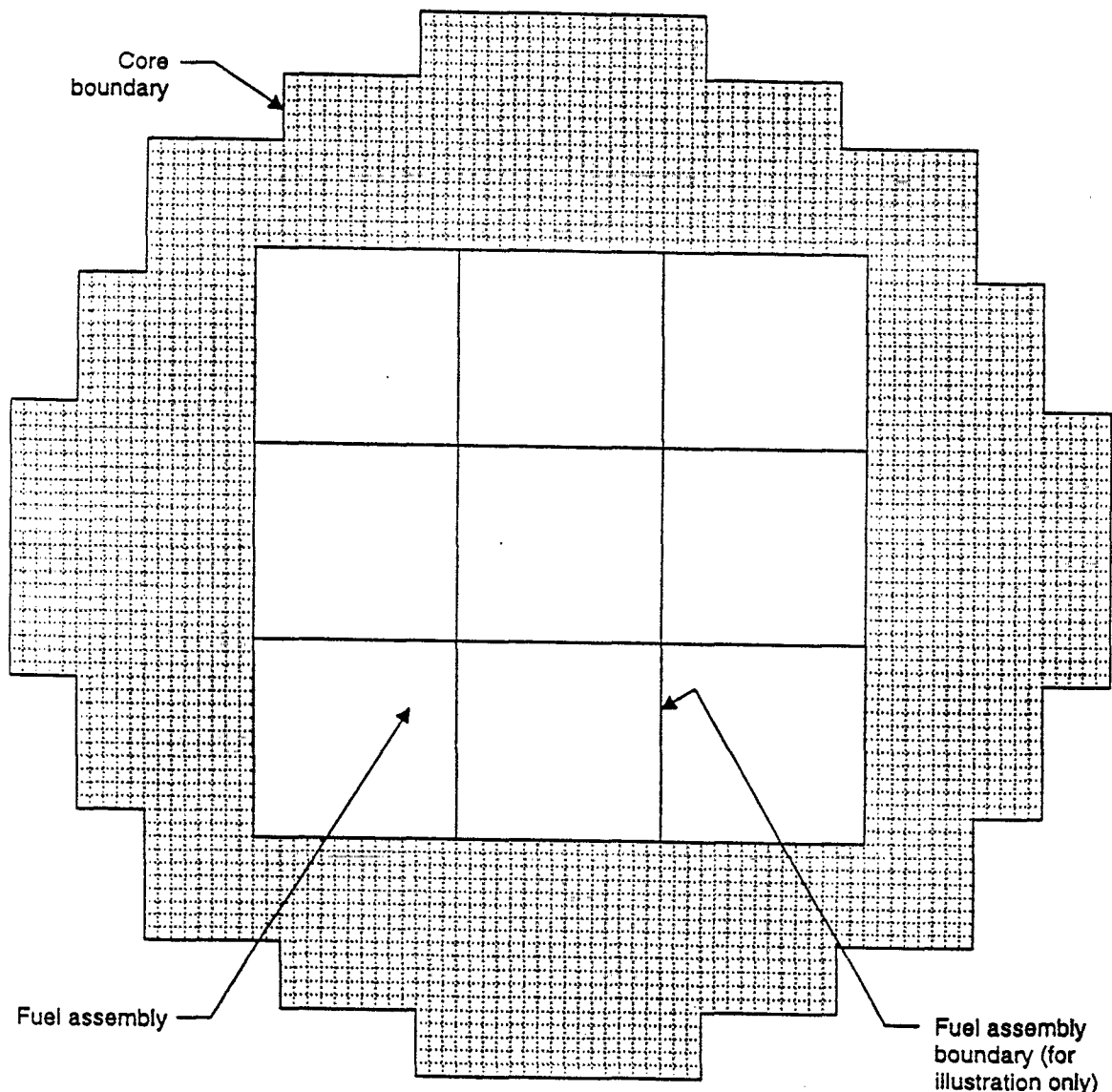


Figure 1. Basic geometry for B&W core XI lattices.

Each of the fuel pins is clad in aluminum and has an enrichment of 2.459 wt.%. The pins in both the central region and the buffer are arranged on a grid with a pitch of 1.63576 cm.

In loading 1, fuel pins occupy all of the lattice positions in the central 9 fuel assemblies. Consequently, there is no distinction between those assemblies and the buffer, and the lattice is uniform. In loading 2, the fuel rods have been removed from 17 positions in each assembly. The location of those positions within the assembly corresponds to the location of the water holes in a normal 15 x 15 assembly. In loading 8, Pyrex rods have been inserted in 16 of the open positions in each assembly, while the central position remains vacant. The progression from loading 1 to loading 2 to loading 8 therefore corresponds to a transition from a uniform lattice to assemblies with water holes to assemblies heavily loaded with discrete burnable absorbers.

Because pin-by-pin fission distributions had been measured in the central assembly of loadings 2 and 8, the number of histories in the MCNP calculations for these three cases was increased to produce standard deviations of approximately 0.1% in the predicted pinwise fission rates. Specifically, each MCNP calculation employed 1,050 generations with 4,000 neutrons per generation, and the first 50 generations were excluded from the statistics. Consequently, the results for each of these cases are based on 4,000,000 active histories.

The normalized pin-by-pin fission distributions predicted for the central assembly in loadings 2 and 8 are compared with the measured distributions in Figures 2 and 3, respectively. The ENDF/B-V distributions for these 2 loadings both produce a slightly better match with the measured distributions than do the corresponding ENDF/B-VI distributions. For the complete set of loadings, however, the two libraries produce comparable results.³³ The root-mean-square (RMS) differences between the ENDF/B-V and ENDF/B-VI fission distributions for loadings 2 and 8 are both 0.016, which indicates that the fission distributions predicted by ENDF/B-V and ENDF/B-VI agree slightly better with each other than either of them does with the measured distributions.

The MCNP eigenvalues for these cases are presented in Table 5. Both ENDF/B-V and ENDF/B-VI produce good agreement with the benchmark values for k_{eff} , although they underpredict it slightly. On average, ENDF/B-V is low by approximately 0.003 Δk , and ENDF/B-VI is low by approximately 0.005 Δk . Both libraries tend to produce an RMS variation of about 2% relative to the measured pin-by-pin fission rates, which is quite acceptable.

These differences are representative of those obtained for other loadings as well.³³ The reactivity difference between the ENDF/B-V and ENDF/B-VI results is due primarily to changes in the cross sections for ^{235}U and ^{238}U . Relative to ENDF/B-V, the ENDF/B-VI cross sections for ^{235}U tend to increase reactivity, while the cross sections for ^{238}U tend to decrease it. The net effect of these tendencies depends upon the enrichment of the fuel and the neutron spectrum, as will be shown in the discussion of data testing for reactor lattices. In this particular case, the net effect is that ENDF/B-VI consistently underpredicts ENDF/B-V by approximately 0.002 Δk .

It has been reported³⁴ recently that the MCNP ENDF/B-V library produces a bias of approximately -0.003 Δk in the calculated k_{eff} in thermal lattices with LEU. If that bias is applied here, ENDF/B-V produces excellent agreement with the benchmark value of k_{eff} (the difference is one standard deviation or less for all 3 cases), and the reactivity difference between ENDF/B-V and ENDF/B-VI increases to approximately 0.005 Δk .

Solutions. The uranium solutions include six HEU solutions, one LEU solution, and five solutions of ^{233}U . Five of the HEU solutions are spheres of uranyl nitrate in light water, and the sixth is a sphere of uranyl fluoride in heavy water. The LEU solution is an annular cylinder of uranyl fluoride in light water, and the solutions of ^{233}U are spheres of

Water Hole	1.107±0.002 1.122±0.013 1.124±0.013	1.026±0.006 1.028±0.012 1.049±0.012	1.000±0.001 1.014±0.012 1.025±0.012	1.025±0.007 1.005±0.012 1.019±0.012	1.026±0.003 1.002±0.011 1.040±0.012	0.980±0.021 0.989±0.011 1.008±0.011	0.983±0.008 0.963±0.011 0.966±0.011
	1.068±0.002 1.080±0.012 1.088±0.012	1.075±0.000 1.096±0.009 1.117±0.010	1.036±0.007 1.049±0.009 1.060±0.009	1.047±0.004 1.045±0.009 1.048±0.009	1.098±0.006 1.074±0.009 1.098±0.009	1.026±0.023 1.018±0.008 1.026±0.009	1.003±0.031 0.969±0.008 0.958±0.008
	Water Hole	1.116±0.012 1.130±0.009 1.139±0.009	1.118±0.011 1.137±0.009 1.117±0.009	Water Hole	1.070±0.010 1.083±0.009 1.070±0.009	0.967±0.010 0.979±0.008 0.990±0.008	
			1.091±0.009 1.071±0.012 1.101±0.012	1.145±0.008 1.152±0.009 1.152±0.009	1.133±0.010 1.128±0.009 1.123±0.009	1.032±0.026 1.019±0.008 1.007±0.008	0.924±0.006 0.987±0.008 0.974±0.008
			Water Hole	1.109±0.007 1.096±0.009 1.087±0.009	1.007±0.014 1.008±0.008 0.974±0.008	0.974±0.026 0.961±0.008 0.949±0.008	
				1.015±0.002 1.010±0.011 1.006±0.012	0.973±0.023 0.980±0.008 0.960±0.008	0.971±0.012 0.955±0.008 0.939±0.008	
					0.970±0.006 0.960±0.012 0.952±0.011	0.950±0.005 0.931±0.008 0.934±0.008	
					Measured ENDF/B-V ENDF/B-VI	0.920±0.013 0.919±0.011 0.934±0.011	

Figure 2. Relative power distribution for B&W core XI load 2.

RMS Difference	
ENDF/B-V	ENDF/B-VI
0.020	0.0024

Water Hole	1.148±0.007 1.152±0.020 1.175±0.020	1.027±0.004 1.050±0.017 1.059±0.017	1.045±0.006 1.039±0.017 1.050±0.017	1.057±0.006 1.021±0.016 1.028±0.016	1.047±0.005 1.066±0.017 1.035±0.017	1.088±0.004 1.072±0.017 1.080±0.017	1.124±0.016 1.124±0.017 1.118±0.017
	1.036±0.005 1.067±0.018 1.102±0.018	0.945±0.007 0.939±0.012 0.965±0.012	1.001±0.006 1.009±0.012 0.998±0.012	0.982±0.021 0.997±0.012 0.991±0.012	0.962±0.008 0.963±0.011 0.962±0.012	1.070±0.014 1.060±0.012 1.063±0.012	1.105±0.009 1.123±0.013 1.104±0.013
		Pyrex Rod	0.901±0.006 0.908±0.011 0.891±0.011	0.900±0.019 0.897±0.011 0.900±0.011	Pyrex Rod	1.001±0.021 0.990±0.011 1.004±0.012	1.087±0.007 1.094±0.012 1.094±0.012
			0.914±0.004 0.924±0.016 0.927±0.016	0.854±0.017 0.866±0.011 0.893±0.011	0.933±0.005 0.909±0.011 0.915±0.011	1.049±0.014 1.035±0.012 1.056±0.012	1.088±0.005 1.120±0.012 1.094±0.012
				Pyrex Rod	0.970±0.012 0.950±0.012 0.959±0.012	1.097±0.020 1.096±0.012 1.106±0.012	1.138±0.015 1.149±0.013 1.135±0.013
					1.071±0.006 1.050±0.016 1.057±0.016	1.140±0.014 1.133±0.013 1.135±0.013	1.195±0.006 1.164±0.013 1.144±0.013
						1.164±0.003 1.150±0.018 1.157±0.017	1.199±0.008 1.198±0.013 1.171±0.013
						Measured ENDF/B-V ENDF/B-VI	1.206±0.011 1.244±0.019 1.215±0.018

RMS Differences

ENDF/B-V ENDF/B-VI

0.016 0.020

Figure 3. Relative power distribution for B&W core XI load 8.

uranyl nitrate in light water. The sphere of HEU uranyl nitrate in heavy water is reflected by heavy water, but none of the other solutions are reflected.

The experiments^{35,36} with the spheres of HEU uranyl nitrate were performed at Oak Ridge National Laboratory (ORNL) in the 1950s and are designated as ORNL-1, ORNL-2, ORNL-3, ORNL-4, and ORNL-10. The enrichment for all five cases is 93.2 wt.%. ORNL-1, ORNL-2, ORNL-3, and ORNL-4 have an outer radius of 34.595 cm, while ORNL-10 has an outer radius of 61.011 cm. The CSEWG benchmarks for these spheres represent them as completely bare with no container. ORNL-1, ORNL-2, ORNL-3, and ORNL-4 contain successively increasing amounts of uranyl nitrate, while the uranyl nitrate in ORNL-10 is more dilute than in ORNL-1. ORNL-2, ORNL-3, and ORNL-4 contain dilute amounts of boron (on the order of 20 to 50 PPM relative to the water), but ORNL-1 and ORNL-10 do not. The leakage in ORNL-1 is approximately 20%, while the leakage in the other three spheres with the same radius is approximately 17%. Although the leakage is lower in the latter three cases, the neutron spectra actually are harder because of the higher concentration of fissile material and the presence of boron. The spectrum for ORNL-10 is softer than that for any of the smaller spheres, because it has nearly three times the volume, contains no boron, and its fissile material is more dilute. Leakage for ORNL-10 is less than 7%.

The CSEWG specifications, unfortunately, do not include any uncertainty in k_{eff} for the ORNL HEU spheres. However, uncertainties of $0.0026 \Delta k$ for ORNL-1 and $0.0023 \Delta k$ for ORNL-2, ORNL-3, and ORNL-4 recently have been established,³⁷ and it is likely that the actual uncertainty for ORNL-10 is about the same size.

The experiment³⁸ with the sphere of uranyl fluoride in heavy water was performed at LANL in the 1950s. The mixture of uranyl fluoride and heavy water is contained inside a spherical shell of stainless steel, and its heavy-water reflector is contained inside a concentric second spherical shell, also made of stainless steel. The inner and outer radii of the inner shell are 22.211 and 22.313 cm, respectively, while the inner and outer radii of the outer shell are 44.411 and 44.665 cm, respectively. The enrichment of the uranium is 93.65 wt.%.

The SHEBA-II experiment^{39,40} was performed at LANL in the 1990s. It contains a uranyl-fluoride solution inside an annular cylinder of 304L stainless steel. The uranyl fluoride contains uranium with an enrichment of approximately 5 wt.%. The stainless-steel container is slightly less than 80 cm tall, and the hollow central column is 5.08 cm wide. The inner radius of the outer wall is approximately 24.4 cm, and the critical height of the solution is 44.8 cm. The inner wall of the container is 0.635 cm thick, while the outer wall is slightly less than 1 cm thick.

The MCNP results for uranium solutions are summarized in Table 6.

ENDF/B-V produces generally good agreement with the benchmark values for k_{eff} for the ORNL HEU spheres, although it has a tendency to underpredict it slightly. ENDF/B-VI tends to underpredict ENDF/B-V by approximately $0.002 \Delta k$. Sensitivity studies indicate that this reduction in k_{eff} is due primarily to differences between the ENDF/B-V and ENDF/B-VI evaluations for ^{235}U and, to lesser extent, for ^{16}O .

Unfortunately, the uncertainty for the benchmark value of k_{eff} for the reflected sphere of uranyl fluoride is so large that no definitive conclusions can be drawn about the relative accuracy of ENDF/B-V and ENDF/B-VI for this experiment. (The ICSBEP benchmarks include other spheres as well as cylinders in the same series of experiments. However, the uncertainties for those other experiments are comparable to that for the one discussed herein.) Nonetheless, the MCNP results demonstrate that ENDF/B-V and ENDF/B-VI produce significantly different results for the combination of uranyl fluoride and heavy water. In particular, the ENDF/B-VI k_{eff} for this case is approximately $0.007 \Delta k$ higher

Table 5. Results for uranium lattices.

Case title	Benchmark k_{eff}	k_{eff}		Δk	
		ENDF/B-V	ENDF/B-VI	ENDF/B-V	ENDF/B-VI
B&W Core XI, Loading 1	1.0007 \pm 0.0012	0.9981 \pm 0.0003	0.9963 \pm 0.0003	-0.0026 \pm 0.0012	-0.0044 \pm 0.0012
B&W Core XI, Loading 2	1.0007 \pm 0.0012	0.9988 \pm 0.0003	0.9964 \pm 0.0003	-0.0019 \pm 0.0012	-0.0043 \pm 0.0012
B&W Core XI, Loading 8	1.0007 \pm 0.0012	0.9965 \pm 0.0003	0.9944 \pm 0.0003	-0.0042 \pm 0.0012	-0.0063 \pm 0.0012

Table 6. Results for uranium solutions.

Case title	Principal Fuel	Benchmark k_{eff}	k_{eff}		Δk	
			ENDF/B-V	ENDF/B-VI	ENDF/B-V	ENDF/B-VI
ORNL-1	HEU	1.0003	1.0005 \pm 0.0006	0.9951 \pm 0.0005	0.0002 \pm 0.0006	-0.0052 \pm 0.0005
ORNL-2	HEU	0.9998	0.9981 \pm 0.0006	0.9968 \pm 0.0006	-0.0017 \pm 0.0006	-0.0030 \pm 0.0006
ORNL-3	HEU	0.9999	0.9961 \pm 0.0006	0.9943 \pm 0.0006	-0.0038 \pm 0.0006	-0.0056 \pm 0.0006
ORNL-4	HEU	0.9992	0.9964 \pm 0.0006	0.9939 \pm 0.0006	-0.0028 \pm 0.0006	-0.0053 \pm 0.0006
ORNL-10	HEU	1.0003	0.9996 \pm 0.0004	0.9972 \pm 0.0004	-0.0007 \pm 0.0004	-0.0031 \pm 0.0006
Uranyl fluoride in D ₂ O	HEU	1.0000 \pm 0.0104	0.9967 \pm 0.0010	1.0040 \pm 0.0009	-0.0033 \pm 0.0105	0.0040 \pm 0.0104
SHEBA-II	LEU	0.9991 \pm 0.0043	1.0115 \pm 0.0008	1.0076 \pm 0.0008	0.0124 \pm 0.0044	0.0085 \pm 0.0044
ORNL-5	²³⁵ U	1.0000 \pm 0.0032	1.0013 \pm 0.0006	0.9970 \pm 0.0006	0.0013 \pm 0.0033	-0.0030 \pm 0.0033
ORNL-6	²³⁵ U	1.0005 \pm 0.0032	1.0013 \pm 0.0006	0.9972 \pm 0.0006	0.0008 \pm 0.0033	-0.0033 \pm 0.0033
ORNL-7	²³⁵ U	1.0006 \pm 0.0032	1.0010 \pm 0.0006	0.9979 \pm 0.0006	0.0004 \pm 0.0033	-0.0027 \pm 0.0033
ORNL-8	²³⁵ U	0.9998 \pm 0.0032	1.0001 \pm 0.0006	0.9967 \pm 0.0006	0.0003 \pm 0.0033	-0.0031 \pm 0.0033
ORNL-9	²³⁵ U	0.9999 \pm 0.0032	0.9999 \pm 0.0006	0.9968 \pm 0.0006	0.0000 \pm 0.0033	-0.0031 \pm 0.0033

than the corresponding ENDF/B-V value. Sensitivity studies indicate that differences between the ENDF/B-V and ENDF/B-VI cross sections for ^{235}U , ^{16}O , and Fe all contribute significantly to the reactivity difference.

Both ENDF/B-V and ENDF/B-VI overpredict the reactivity for SHEBA-II, although ENDF/B-VI does so by a substantially smaller margin. The difference in reactivity is due primarily to differences in cross sections for ^{238}U and, to a lesser extent, for ^{16}O .

Overall, ENDF/B-V tends to underpredict k_{eff} slightly for the HEU uranyl-nitrate solutions, and ENDF/B-VI tends to underpredict it by a slightly larger margin. On average, ENDF/B-V produces a k_{eff} of approximately 0.997 for the ORNL HEU spheres, while ENDF/B-VI produces a value of approximately 0.995. In contrast, both ENDF/B-V and ENDF/B-VI overpredict the reactivity for the LEU uranyl-fluoride solution in SHEBA-II. ENDF/B-VI continues to underpredict ENDF/B-V, but the difference has increased to approximately 0.004 Δk . The reactivity difference for the reflected sphere of uranyl fluoride in heavy water reverses the pattern between the two libraries, however: ENDF/B-VI produces a value for k_{eff} that is approximately 0.007 Δk higher than the corresponding ENDF/B-V value. Unfortunately, the large uncertainty associated with this last benchmark precludes a conclusive determination of which library produces the better result.

The pattern reversal between the case with uranyl fluoride in heavy water and the other cases may be related to the neutron spectrum. Even though the former case is reflected, its leakage is substantially higher than that of any of the other solutions. Leakage for that case is slightly more than 40%, whereas the leakage for SHEBA-II is slightly less than 25%, and the leakage for all of the ORNL HEU spheres is less than 20%. Furthermore, the moderator and reflector for the uranyl-fluoride sphere are heavy water, whereas the moderator for the ORNL HEU spheres and for SHEBA-II is light water. Consequently, the neutron spectrum for the uranyl-fluoride sphere is substantially harder than the spectra for the other solutions.

The experiments^{35,36} with ^{235}U uranyl-nitrate solutions were performed at ORNL in the 1950s and are designated ORNL-5, ORNL-6, ORNL-7, ORNL-8, and ORNL-9. The uranium was enriched to 97.7 wt.% in ^{235}U . All five of the solutions are enclosed inside a thin, spherical shell of aluminum-1100. The shell has an inner radius of 34.595 cm and is 0.32 cm thick. (It is worth noting that the outer radius of the ^{235}U uranyl nitrate solutions in ORNL-5 through ORNL-9 is the same as that of the HEU uranyl-nitrate solutions for ORNL-1 through ORNL-4.) ORNL-5 contains no boron, while ORNL-6 through ORNL-9 contain successively increasing amounts of boron. The concentration of uranyl nitrate, although relatively dilute for all five cases, increases from one case to the next to offset the negative reactivity introduced by the increase in boron. However, the uranyl nitrate remains sufficiently dilute that the leakage from these spheres is only about 2%.

The results for ORNL-5 through ORNL-9 are included in Table 6. Generally speaking, both the ENDF/B-V and the ENDF/B-VI values for k_{eff} fall within a single standard deviation of the benchmark k_{eff} . However, a pattern is evident: the ENDF/B-VI values are consistently about 0.003 Δk lower than the ENDF/B-V values. As was mentioned earlier, the ENDF/B-VI evaluation for ^{235}U differs only slightly from the corresponding ENDF/B-V evaluation. Therefore, the difference in reactivity is not attributable to differences in the cross sections for ^{235}U . Sensitivity studies demonstrated that differences between the cross sections for ^{16}O are responsible for essentially the entire reactivity difference. However, the mechanism for this effect is not obvious. The leakage is too low for differences in the total ^{16}O cross section at high energies to have much effect, and ^{16}O is too weak an absorber to produce that reactivity change directly. The difference may be due to interactions between ^{16}O and other isotopes, most likely ^{235}U .

Plutonium Critical Experiments

The plutonium critical experiments are summarized in Table 7. They include metal spheres, mixed-oxide (MOX) lattices, and plutonium-nitrate solutions. Fast neutrons produce most of the fissions in the metal systems, while thermal neutrons produce most of the fissions in the lattices and the solutions.

The metal and solution systems were critical, but the MOX lattice experiments all were slightly supercritical. However, the benchmark values for k_{eff} for four of the MOX experiments are less than unity, because they incorporate adjustments, given in the benchmark specifications, to account for PuO_2 particle effects.

Metal Spheres. The metallic plutonium systems include two bare spheres, a sphere reflected by normal uranium, and a sphere immersed in water. The distinction between the two bare spheres is the amount of ^{240}Pu that they contain. All of these experiments were performed at LANL during the 1950s and 1960s.

Jezebel^{23,41,42} is a bare sphere of delta-phase plutonium that contains 4.5 at.% ^{240}Pu . It has a radius of 6.3849 cm and a density of 15.61 g/cm³.

Jezebel-240⁴² also is a bare sphere of delta-phase plutonium, but it contains 20.1 at.% ^{240}Pu . It has a radius of 6.6595 cm and a density of 15.73 g/cm³.

FLATTOP-Pu^{23,26} is a sphere of delta-phase plutonium encased inside a spherical shell of normal uranium. The plutonium sphere contains 4.83 at.% ^{240}Pu . It has an outer radius of 4.533 cm and a density of 15.53 g/cm³, and the uranium shell has an outer radius of 24.13 cm and a density of 19.00 g/cm³.

The water-reflected plutonium sphere⁴³ contains alpha-phase plutonium with 5.20 at.% ^{240}Pu . It has an outer radius of 4.1217 cm and a density of 19.74 g/cm³. The water that surrounds it is neutronically infinite. Although some of the fissions that occur in the sphere are produced by thermal neutrons, the majority of the fissions is produced by fast neutrons.

The results for the metallic plutonium spheres are presented in Table 8. ENDF/B-V and ENDF/B-VI produce statistically identical values for k_{eff} for the first three spheres, and the values for the water-reflected sphere differ by only 0.002 Δk . Furthermore, the results are in excellent agreement with the benchmark values for k_{eff} . All of the calculated values are within two standard deviations of the benchmark value, and four of them are within one standard deviation. Sensitivity studies demonstrated that the difference between the ENDF/B-V and ENDF/B-VI results for the water-reflected sphere are due not to the plutonium isotopes but rather to differences in the cross-section libraries for ^{16}O . This behavior appears to arise from interactions between plutonium and oxygen, however, because there was no corresponding difference in the results for the water-reflected HEU sphere or cube.

Lattices. The MOX lattice experiments^{44,45} were performed by Battelle Pacific Northwest Laboratory (PNL) during the 1970s. They contain MOX fuel pins arranged in a uniform lattice with a square pitch, in a roughly cylindrical arrangement. The fuel pins contain 2 wt.% PuO_2 , and the plutonium nominally contains 8 at.% ^{240}Pu . The benchmark specifications, however, correspond to 7.73 at.% ^{240}Pu . The active length of the fuel pins is 91.44 cm, and they have an outer radius of 0.6414 cm. The pins are clad in zirconium with an outer radius of 0.7176 cm, and they are supported by an aluminum platform. A lead radiation shield rests on top of the pins. The water in which the pins are immersed is neutronically infinite on the bottom and sides of the lattice, and the water height above the radiation shield ranges from 2.29 to 15.24 cm, depending on the particular experiment. The six cases involve three different pitches, and there is a borated and (essentially) unborated case at each pitch. More details about these cases are presented in Table 9. The

Table 7. Summary of plutonium benchmark cases.

Case title	²⁴⁰ Pu Content	Moderator	Reflector	Basic geometry	Source	Benchmark k_{eff}
Jezebel	4.50 at. %	None	None	Sphere	ICSBEP	1.0000 ± 0.0020
Jezebel-240	20.10 at. %	None	None	Sphere	ICSBEP	1.0000 ± 0.0020
FLATTOP-Pu	4.83 at. %	None	Normal U	Nested spheres	ICSBEP ^a	1.0000 ± 0.0030
Pu sphere in water	5.20 at. %	None	Water	Nested spheres	ICSBEP	1.0000 ± 0.0010
PNL-30	7.73 at. %	Water	Water	Uniform lattice	CSEWG	1.0002
PNL-31	7.73 at. %	Water	Water	Uniform lattice	CSEWG	1.0001
PNL-32	7.73 at. %	Water	Water	Uniform lattice	CSEWG	0.9985
PNL-33	7.73 at. %	Water	Water	Uniform lattice	CSEWG	0.9984
PNL-34	7.73 at. %	Water	Water	Uniform lattice	CSEWG	0.9983
PNL-35	7.73 at. %	Water	Water	Uniform lattice	CSEWG	0.9976
PNL-1	4.58 at. %	Water	None	Sphere	CSEWG	1.0
PNL-2	4.58 at. %	Water	None	Sphere	CSEWG	1.0
PNL-3	4.18 at. %	Water	Cadmium	Nested spheres	ICSBEP	1.0000 ± 0.0052
PNL-4	4.18 at. %	Water	Cadmium	Nested spheres	ICSBEP	1.0000 ± 0.0052
PNL-5	4.15 at. %	Water	None	Sphere	CSEWG	1.0
Pu nitrate sphere	3.12 at. %	Water	Water	Nested spheres	ICSBEP	1.0000 ± 0.0047
Pu nitrate sphere, high Pu	3.12 at. %	Water	Water	Nested spheres	ICSBEP	1.0000 ± 0.0047
Pu nitrate sphere, low ²⁴⁰ Pu	0.54 at. %	Water	Water	Nested spheres	ICSBEP	1.0000 ± 0.0047

^a Formal approval has not yet been granted for this specification.

Table 8. Results for metallic plutonium spheres.

Case title	Benchmark k_{eff}	k_{eff}		Δk	
		ENDF/B-V	ENDF/B-VI	ENDF/B-V	ENDF/B-VI
Jezebel	1.0000 ± 0.0020	0.9975 ± 0.0006	0.9975 ± 0.0006	-0.0025 ± 0.0021	-0.0025 ± 0.0021
Jezebel-240	1.0000 ± 0.0020	0.9994 ± 0.0006	0.9996 ± 0.0006	-0.0006 ± 0.0021	-0.0004 ± 0.0011
FLATTOP-Pu	1.0000 ± 0.0030	1.0030 ± 0.0007	1.0039 ± 0.0007	0.0030 ± 0.0031	0.0039 ± 0.0031
Pu sphere in water	1.0000 ± 0.0010	0.9999 ± 0.0008	0.9978 ± 0.0007	-0.0001 ± 0.0013	-0.0022 ± 0.0012

Table 9. Critical configurations for MOX lattices.

Case	Fuel Pins	Pitch (cm)	Soluble Boron (PPM)
PNL-30	469	1.77800	2
PNL-31	761	1.77800	681
PNL-32	195	2.20914	1
PNL-33	761	2.20914	1090
PNL-34	160	2.51447	2
PNL-35	689	2.51447	767

CSEWG specifications for these cases do not include a stated uncertainty. It is assumed, therefore, that the uncertainty in k_{eff} is small.

The results from these cases are summarized in Table 10. Three trends are observable: (1) ENDF/B-VI consistently underpredicts ENDF/B-V, by about $0.006 \Delta k$, (2) the values of k_{eff} for the borated cases are consistently higher than those for the unborated cases at the same pitch, and (3) the value of k_{eff} increases as the pitch increases. Overall, ENDF/B-VI produces marginally better agreement with these benchmarks than ENDF/B-V does. Relative to the benchmark k_{eff} , the sample means for the ENDF/B-V and ENDF/B-VI results are given by, respectively,

$$\bar{k}_{eff}^V = k_{eff}^{bmk} + 0.0071 \pm 0.0068 \quad (1)$$

and

$$\bar{k}_{eff}^{VI} = k_{eff}^{bmk} + 0.0009 \pm 0.0063 \quad (2)$$

where k_{eff}^{bmk} is the benchmark value for k_{eff} . Although the bias for ENDF/B-VI is smaller than that for ENDF/B-V, the standard deviation for both of them is quite large.

Sensitivity studies indicate that the consistent difference between the ENDF/B-V and ENDF/B-VI results is due primarily to differences in the cross sections for ^{16}O and ^{239}Pu . Differences in the cross sections for ^{235}U tend to increase k_{eff} slightly for ENDF/B-VI relative to ENDF/B-V, while differences in the cross sections for ^{238}U and ^{240}Pu tend to decrease it slightly. However, these differences tend to offset each other, and, in any case, the impact of the cross-section differences on k_{eff} for any one of these three isotopes is only about $0.001 \Delta k$.

The differences between the calculated values of k_{eff} for borated and unborated cases at the same pitch are about $0.005 \Delta k$ for both ENDF/B-V and ENDF/B-VI. The leakage for these experiments is very low (approximately 2% for the unborated cases and less than 1% for the borated cases). Because the presence of the boron tends to harden the spectrum, the conversion ratio increases by about 10% for a borated case relative to the corresponding unborated case. This pattern suggests that spectral effects may be responsible for the observed differences. On the other hand, this trend also could be explained by a systematic underestimate of the boron level in the borated cases.

The trend of increasing k_{eff} with pitch also could be a spectral effect, because the spectrum becomes increasingly softer as the pitch (and hence the moderator-to-fuel ratio) increases. In particular, the conversion ratio decreases by more than 40% in going from the tightest pitch to the loosest. However, the variation of k_{eff} with pitch is essentially the same for ENDF/B-VI as it is for ENDF/B-V: the value of k_{eff} for the loosest pitch is approximately $0.010 \Delta k$ higher than that for the tightest pitch for both borated and unborated cases. This behavior suggests either that a deficiency in the ENDF/B-V cross sections also exists in their ENDF/B-VI counterparts or that there is a problem with the benchmark specifications.

The only definitive conclusion that can be drawn from these results is that ENDF/B-VI consistently produces a value of k_{eff} for MOX lattices that is approximately $0.006 \Delta k$ lower than the corresponding ENDF/B-V value.

Solutions. Five unreflected and three water-reflected spheres of plutonium nitrate were studied. All of the experiments^{46,47} upon which these benchmarks are based were performed by PNL during the 1960s. The CSEWG benchmark specifications for PNL-1 through PNL-5 represent them simply as bare spheres of plutonium nitrate. However, the experiments upon which PNL-3 and PNL-4 are based recently have been evaluated as part of the ICSBEP, and it has been suggested⁴⁸ that those two CSEWG benchmarks be revised

to conform to the ICSBEP specifications. Consequently, the ICSBEP specifications have been used herein for PNL-3 and PNL-4. The principal difference between the two sets of specifications is that the ICSBEP benchmark retains the stainless steel sphere that encloses the solution and its cadmium cover.

The unreflected spheres differ primarily with respect to the concentration of plutonium nitrate, although there also are variations in size and ^{240}Pu content.

The outer radius of the bare spheres for PNL-1 and PNL-2 is 19.509 cm, and the plutonium contains 4.58 at.% ^{240}Pu . PNL-1 contains approximately 38.8 g/l of plutonium, while PNL-2 contains approximately 171.7 g/l.

The outer radius of the sphere for PNL-3 and PNL-4 is 22.7 cm, and the plutonium contains 4.18 at.% ^{240}Pu . As noted above, the plutonium-nitrate solution is contained in a stainless steel shell that is enclosed by a cadmium cover. Both the stainless steel shell and the cadmium cover are quite thin, however; the shell is approximately 0.13 cm thick and the cover is only .05 cm thick. PNL-3 contains approximately 22.4 g/l of plutonium, while PNL-4 contains approximately 27.5 g/l. Both of these concentrations are significantly more dilute than those in PNL-1 and (especially) PNL-2.

The outer radius of the bare sphere for PNL-5 is 20.1265 cm, and the plutonium contains 4.15 at.% ^{240}Pu . The plutonium density in PNL-5 is approximately 43.2 g/l, which is only about 11% higher than that for PNL-1.

The three water-reflected spheres all have the same radii but different concentrations of plutonium. In addition, one of them contains a different fraction of ^{240}Pu than the other two. The outer radius of the plutonium-nitrate solution is 17.79 cm, and the thickness of the stainless-steel shell that contains it is less than 0.13 cm. The water reflector is neutronically infinite for all three cases.

The first water-reflected plutonium-nitrate sphere has a plutonium density of approximately 29.57 g/l, and the plutonium contains 3.12 at.% ^{240}Pu . The second sphere has the same ^{240}Pu fraction as the first, but its plutonium density is 39.38 g/l. The third sphere has a slightly lower plutonium density (26.27 g/l) than the first, but its plutonium contains only 0.54 at.% ^{240}Pu . Therefore, relative to the first case, the second case contains significantly more plutonium, while the third case contains significantly less ^{240}Pu .

As the results in Table 11 demonstrate, ENDF/B-V tends to overestimate the value of k_{eff} substantially; the computed k_{eff} is high for all of the cases, and the difference exceeds 0.005 Δk for seven of the eight. This pattern also has been observed for earlier versions of ENDF/B. However, ENDF/B-VI produces a striking improvement: its values for k_{eff} are 0.006 to 0.010 Δk lower than those from ENDF/B-V and are within $\pm 0.005 \Delta k$ of unity for seven of the eight cases. (A criterion of $\pm 0.005 \Delta k$ seems reasonable for these cases, because that is the approximate size of the uncertainty given for the benchmark value of k_{eff} in the ICSBEP specifications for PNL-3 and PNL-4. Although the CSEWG specifications do not include uncertainties, it is likely that the actual uncertainties would be about the same as those for PNL-3 and PNL-4 because of the similarity of the cases.) Sensitivity studies indicate that the improvement is due primarily to differences between the ENDF/B-V and ENDF/B-VI cross sections for ^{239}Pu , ^{16}O , and, to a lesser extent, ^{240}Pu and Fe.

The pattern that was observed for MOX lattices continues to hold for these plutonium-nitrate solutions, but it is more extreme; ENDF/B-VI consistently produces a value for k_{eff} that is approximately 0.0075 Δk lower than its ENDF/B-V counterpart. For these solutions, it is quite clear that ENDF/B-VI produces results that agree much better with the benchmark values of k_{eff} than do those produced by ENDF/B-V.

Table 10. Results for MOX lattices.

Case title	Benchmark k_{eff}	k_{eff}		Δk	
		ENDF/B-V	ENDF/B-VI	ENDF/B-V	ENDF/B-VI
PNL-30	1.0002	0.9979 ± 0.0008	0.9917 ± 0.0007	-0.0023 ± 0.0008	-0.0085 ± 0.0007
PNL-31	1.0001	1.0023 ± 0.0007	0.9968 ± 0.0007	0.0022 ± 0.0007	-0.0033 ± 0.0007
PNL-32	0.9985	1.0049 ± 0.0007	0.9970 ± 0.0007	0.0064 ± 0.0007	-0.0015 ± 0.0007
PNL-33	0.9984	1.0105 ± 0.0007	1.0042 ± 0.0007	0.0121 ± 0.0007	0.0058 ± 0.0007
PNL-34	0.9983	1.0084 ± 0.0007	1.0018 ± 0.0007	0.0101 ± 0.0007	0.0035 ± 0.0007
PNL-35	0.9976	1.0118 ± 0.0008	1.0061 ± 0.0007	0.0142 ± 0.0008	0.0085 ± 0.0007

Table 11. Results for plutonium solutions.

Case title	Benchmark k_{eff}	k_{eff}		Δk	
		ENDF/B-V	ENDF/B-VI	ENDF/B-V	ENDF/B-VI
PNL-1	1.0	1.0146 ± 0.0010	1.0077 ± 0.0009	0.0146 ± 0.0010	0.0077 ± 0.0010
PNL-2	1.0	1.0060 ± 0.0010	0.9999 ± 0.0010	0.0060 ± 0.0010	-0.0001 ± 0.0010
PNL-3	1.0000 ± 0.0052	1.0020 ± 0.0008	0.9953 ± 0.0008	0.0020 ± 0.0053	-0.0047 ± 0.0053
PNL-4	1.0000 ± 0.0052	1.0071 ± 0.0008	0.9994 ± 0.0008	0.0071 ± 0.0053	-0.0006 ± 0.0053
PNL-5	1.0	1.0081 ± 0.0010	1.0001 ± 0.0009	0.0081 ± 0.0010	0.0001 ± 0.0009
Pu nitrate sphere	1.0000 ± 0.0047	1.0121 ± 0.0007	1.0045 ± 0.0008	0.0121 ± 0.0048	0.0045 ± 0.0048
Pu nitrate sphere, high Pu	1.0000 ± 0.0047	1.0082 ± 0.0009	0.9994 ± 0.0008	0.0082 ± 0.0048	-0.0006 ± 0.0048
Pu nitrate sphere, low ^{240}Pu	1.0000 ± 0.0047	1.0076 ± 0.0008	0.9995 ± 0.0008	0.0076 ± 0.0048	-0.0005 ± 0.0048

DATA TESTING: THERMAL-REACTOR LATTICES

ENDF/B-V generally has predicted the neutronic behavior of light-water-reactor (LWR) lattices very accurately. Consequently, comparisons between ENDF/B-V and ENDF/B-VI results for LWR lattices may provide a good indication of how successfully ENDF/B-VI will predict the neutronic behavior of such lattices. Comparisons also have been made for lattices from a variety of other thermal-reactor types. In addition to PWRs and boiling water reactors (BWRs), the reactor types include Russian RBMK reactors, modular high-temperature gas-cooled reactors (MHTGRs), CANDU heavy-water reactors, and heavy-water production reactors (HWPRs). The cases are summarized in Table 12.

Table 12. Summary of thermal-reactor lattices.

Case title	Lattice description
NB-1	Aluminum-clad UO_2 pin in water (TRX T6)
NB-4	Idealization of a "typical" PWR pin cell
NB-5	Aluminum-clad UO_2 pin in water (HiC-13)
PWR OFA pin cell	"Optimized" PWR pin cell at beginning of life (BoL)
Standard PWR pin cell	Standard PWR pin cell at BoL
NB-2	MOX pin cell with soft spectrum (PNL-33)
PWR OFA MOX pin cell	"Optimized" PWR MOX pin cell at BoL
Standard PWR MOX pin cell	Standard PWR MOX pin cell at BoL
BWR bundle, unrodded	8x8 BWR fuel bundle at BoL
BWR bundle, rodded	8x8 BWR fuel bundle at BoL, with control rod inserted
BWR bundle, depleted	8x8 BWR fuel bundle, depleted to 25 MW-d/kg
RBMK fuel cell	Fuel cell for Russian RBMK reactor at BoL
MHTGR cell	Standard core block for MHTGR production reactor at BoL
CANDU cluster	Fuel cluster cell for CANDU reactor at BoL
Modified Mark 22 cell	HWPR fuel cell at BoL
Modified Mark 22 supercell	HWPR supercell with 6 fuel cells and a control-rod cell at BoL

All of these cases employ reflective boundary conditions, and therefore they have no leakage. Furthermore, they all are axially uniform. Consequently, they are effectively two-dimensional.

As was noted previously, ENDF/B-VI libraries for MCNP currently are available only at 300 K. Consequently, the comparisons were limited to "cold" conditions (i.e., room temperature and pressure). However, some parameters of considerable importance for reactor safety are determined at cold conditions (e.g., cold shutdown margin). Furthermore, for several of the lattices, the only significant difference between hot and cold conditions is the additional Doppler broadening of resonances. Even for LWRs, the two main distinguishing features between cold and hot conditions are the differences in Doppler feedback and water density.

No correction has been applied to any of these results to account for the recent report³⁴ that the MCNP ENDF/B-V library systematically underestimates reactivity for thermal LEU systems. If such a correction were included, it is anticipated that the ENDF/B-V values for k_{∞} would increase by approximately $0.003 \Delta k$ for LEU and normal-uranium lattices.

Furthermore, it is possible that it would increase even more for thermal lattices with significant amounts of plutonium, because the harder spectrum in such lattices produces higher fluxes in the energy range where low-lying epithermal ^{238}U capture resonances occur.

PWR Lattices

Comparisons were made for infinite lattices of both once-through (" UO_2 ") and MOX pin cells. Five different UO_2 lattices and three different MOX lattices were studied.

UO_2 Lattices. Three of these lattices are "numerical benchmarks" that have been defined elsewhere.^{49,50} These numerical benchmarks are of interest because they represent a range of spectra that more than spans the range normally seen in LWRs. The other two lattices are based on actual PWR designs.

Numerical benchmark 1 (NB-1) is an idealization of case T6 in the TRX critical experiments.⁵¹ It corresponds to an infinite hexagonal lattice of identical UO_2 fuel pins clad in aluminum and immersed in water. The uranium is only slightly enriched (1.3 wt.%), and the fuel pin has an outer radius of 0.4864 cm. The cladding is 0.0889 cm thick, and the cell pitch is 1.5578 cm. The combination of low fuel enrichment and a relatively high moderator-to-fuel ratio produces a spectrum that is significantly softer than that for a typical PWR pin cell.

NB-4 is an idealization of a "typical" PWR pin cell, although the water that surrounds the fuel pin contains no boron. NB-4 corresponds to an infinite square lattice of identical UO_2 fuel pins clad in zirconium. The enrichment of the uranium is 2.75 wt.%, and the outer radius of the fuel pin is 0.5080 cm. The cladding is 0.08674 cm thick, and the cell pitch is 1.4605 cm.

NB-5 is an idealization of the HiC-13 critical experiment.⁵² It corresponds to an infinite hexagonal lattice of UO_2 fuel pins clad in aluminum and immersed in water. The enrichment of the uranium is 3.05 wt.%, and the outer radius of the fuel is 0.4675 cm. The thickness of the cladding is 0.0615 cm, and the cell pitch is 1.166 cm. This very tight pitch produces a low moderator-to-fuel ratio, and the spectrum therefore is significantly harder than that for a typical PWR pin cell.

The results for NB-1, NB-4, and NB-5 are presented in Table 13, where the reactivity difference is defined as

$$\Delta\rho \equiv \frac{k_{eff}^{VI} - k_{eff}^V}{k_{eff}^{VI} k_{eff}^V} = \frac{1}{k_{eff}^V} - \frac{1}{k_{eff}^{VI}} \quad (3)$$

Although on average the agreement between ENDF/B-V and ENDF/B-VI is quite good, there is a trend to the difference. The ENDF/B-VI value for k_{eff} is significantly lower than the corresponding ENDF/B-V value for NB-1, but the reverse is true for NB-4 and NB-5. This pattern could be attributable either to the difference in enrichment or to the difference in moderator-to-fuel ratio.

To resolve that question, further studies were performed for two sets of PWR UO_2 pin cells. Within each set, the dimensions were held fixed, but the enrichment was changed. The enrichments ranged from as low as 0.711 wt.% (normal uranium) to as high as 3.9 wt.%.

The first set of pin cells is based on a numerical benchmark for the Doppler coefficient of reactivity,⁵³ although the atomic number densities were increased to reflect the change from hot to cold conditions. These pin cells are based on an "optimized" fuel

Table 13. Results for UO_2 numerical benchmarks.

Case title	k_{∞} ENDF/B-VI	k_{∞} ENDF/B-V	$\Delta\rho$
NB-1	1.1392 ± 0.0006	1.1432 ± 0.0006	-0.0031 ± 0.0007
NB-4	1.3399 ± 0.0008	1.3383 ± 0.0008	0.0009 ± 0.0007
NB-5	1.1389 ± 0.0006	1.1374 ± 0.0006	0.0012 ± 0.0007

assembly (OFA) design that has been used in both initial and reload cycles of several PWRs. The outer radius of the fuel rod is 0.39306 cm, the cladding is 0.06496 cm thick, and the cell pitch is 1.26209 cm. This fuel-pin radius is somewhat smaller than that for the corresponding conventional design, and it produces a higher moderator-to-fuel ratio and therefore a somewhat softer spectrum. The fuel pin is clad in zirconium and is immersed in water that contains 1400 PPM of soluble boron.

The second set of pin cells is the same as the first, except that the outer radius of the fuel pin and the thickness of the cladding have been changed to 0.41169 cm and 0.06420 cm, respectively. These changes produce a pin cell that corresponds very closely to a standard PWR design.

The results for these cases are presented in Table 14. The reactivity difference between the ENDF/B-V and ENDF/B-VI results follows the same pattern for both sets of pins: the difference becomes increasingly more positive as the enrichment increases. The moderator-to-fuel ratio does have a small effect, however, because the reactivity difference at a given enrichment is consistently more positive for the standard design than for the OFA design.

Table 14. Results for PWR UO_2 pin cells.

Enrichment (w/o)	Lattice	k_{∞} ENDF/B-VI	k_{∞} ENDF/B-V	$\Delta\rho$
3.9	OFA	1.2337 ± 0.0006	1.2337 ± 0.0006	0.0000 ± 0.0006
3.1	OFA	1.1593 ± 0.0006	1.1596 ± 0.0006	-0.0002 ± 0.0006
2.4	OFA	1.0680 ± 0.0006	1.0689 ± 0.0006	-0.0008 ± 0.0007
1.6	OFA	0.9138 ± 0.0005	0.9160 ± 0.0005	-0.0026 ± 0.0008
0.711	OFA	0.6064 ± 0.0004	0.6080 ± 0.0004	-0.0043 ± 0.0015
3.9	Standard	1.2489 ± 0.0006	1.2467 ± 0.0006	0.0014 ± 0.0005
3.1	Standard	1.1773 ± 0.0006	1.1768 ± 0.0006	0.0004 ± 0.0006
2.4	Standard	1.0928 ± 0.0007	1.0925 ± 0.0007	0.0003 ± 0.0008
1.6	Standard	0.9429 ± 0.0006	0.9447 ± 0.0006	-0.0020 ± 0.0010
0.711	Standard	0.6380 ± 0.0004	0.6386 ± 0.0004	-0.0015 ± 0.0014

Sensitivity studies indicate that the reactivity difference is due primarily to competition between ^{235}U and ^{238}U . The ENDF/B-VI evaluation for ^{235}U produces a more positive reactivity contribution for these lattices than does the corresponding ENDF/B-V evaluation, while the ENDF/B-VI evaluation for ^{238}U produces a more negative reactivity contribution than ENDF/B-V. As a result, ENDF/B-VI tends to predict lower reactivity than ENDF/B-V for normal-uranium or slightly enriched UO_2 fuel cells, but that difference becomes less negative as the enrichment increases and eventually becomes positive.

MOX Lattices. Three different infinite lattices of MOX pin cells were studied. One of them has been defined elsewhere^{49,50} as a "numerical benchmark," while the other two lattices are based on the same OFA and standard designs that were used for the UO₂ lattices discussed previously.

NB-2 is an idealization of the PNL-33 critical experiment^{44,45} that was described earlier. Apart from the fact that NB-2 is two-dimensional and PNL-33 is three-dimensional, the principal difference between them is that the former corresponds to an infinite lattice of fuel cells, while the latter contains a finite number of cells. The other two MOX lattices⁵⁴ simply replace the UO₂ fuel pin in the corresponding lattice with a MOX pin. A significant distinction between NB-2 and the other two MOX lattices is the isotopic composition of the plutonium. In NB-2, the plutonium is primarily ²³⁹Pu; ²⁴⁰Pu accounts for slightly less than 8 at.% of the plutonium, and there are only trace amounts of ²⁴¹Pu and ²⁴²Pu. The plutonium in the OFA and standard MOX lattices, in contrast, corresponds closely to that in discharged UO₂ fuel and contains 45 at.% ²³⁹Pu, 30 at.% ²⁴⁰Pu, 15 at.% ²⁴¹Pu, and 10 at.% ²⁴²Pu.

The results for the MOX pin cells are presented in Table 15. They appear to be independent of the moderator-to-fuel ratio as well as the plutonium isotopics. ENDF/B-VI produces essentially the same reactivity as ENDF/B-V for the PWR cases with 2 wt.% PuO₂, but it produces significantly lower reactivity for the PWR cases with 1 wt.% and for NB-2. Sensitivity studies demonstrated that this behavior is not due to differences in the plutonium cross sections. Instead, it is due primarily to spectral variations and differences between the evaluations for ²³⁸U.

Table 15. Results for MOX pin cells.

PuO ₂ Content (wt.%)	Lattice	k _∞ , ENDF/B-VI	k _∞ , ENDF/B-V	Δρ
2.0	NB-2	1.1685 ± 0.0007	1.1720 ± 0.0008	-0.0026 ± 0.0008
1.0	OFA	0.9045 ± 0.0005	0.9069 ± 0.0005	-0.0029 ± 0.0009
2.0	OFA	1.0178 ± 0.0006	1.0177 ± 0.0007	0.0001 ± 0.0009
1.0	Standard	0.9236 ± 0.0006	0.9212 ± 0.0006	-0.0028 ± 0.0010
2.0	Standard	1.0289 ± 0.0007	1.0277 ± 0.0006	-0.0011 ± 0.0009

BWR Lattice

Calculations were performed for an infinite lattice of identical BWR fuel bundles at three different conditions: unrodded at beginning of life (BoL), rodded at BoL, and unrodded at a bundle-averaged uranium burnup of 25 MW·d/kg. The bundle is an idealization of bundle type 4 for Peach Bottom Unit 2, which was an 8 x 8 design with one internal water hole and 5 gadolinia-loaded fuel pins.⁵⁵ The average enrichment for the bundle at BoL is 2.74 wt.%. In the idealization, the fuel pins are clad in zirconium, and the hollow rod in the water hole also is made of zirconium. The rodded case is identical to the unrodded case except that a control rod with B₄C rodlets clad in stainless steel has been inserted in the wide water gaps.

The isotopics for the depleted bundle were taken from a study⁵⁶ of boron-retention requirements following a severe accident in a BWR. It should be noted, however, that in that study fission products were not represented explicitly. Instead, they were represented by two pseudoisotopes with fixed microscopic cross sections, and the MCNP calculation

for the depleted BWR lattice also employed that representation. Consequently, the results of the calculations for this bundle do not involve actual ENDF/B-V or ENDF/B-VI fission products.

A schematic of the bundle is shown in Figure 4, and the geometry of the rodged bundle is shown in Figure 5.

Wide-
Wide
Corner

4	3	2	2	2	2	2	3
3	2	1	5	1	1	1	2
2	1	1	1	1	1	5	1
2	5	1	1	1	1	1	1
2	1	1	1	Water Rod	1	1	1
2	1	1	1	1	1	1	1
2	1	5	1	1	1	5	1
3	2	1	1	1	1	1	2

Narrow-
Narrow
Corner

Rod Type	Enrichment (wt.% ^{235}U)	Gadolinia (wt.% Gd_2O_3)	Number of Rods
1	3.01	0	39
2	2.22	0	14
3	1.87	0	4
4	1.45	0	1
5	3.01	3.0	5
Water Rod	—	—	1

Figure 4. Bundle type 4 for Peach Bottom unit 2.

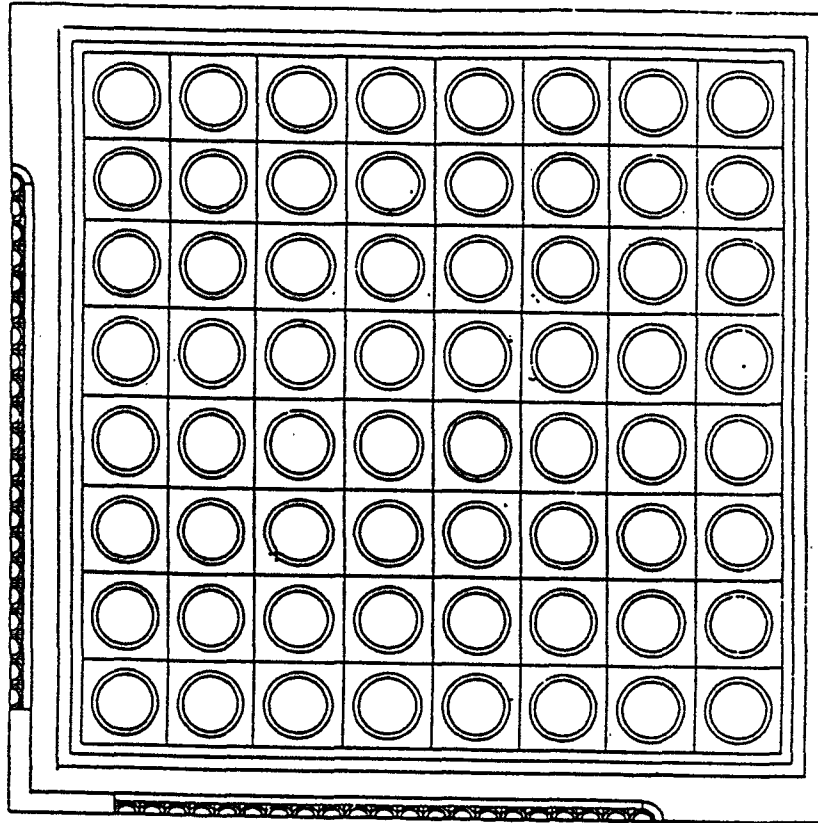


Figure 5. Rodded BWR bundle.

The results from the calculations are presented in Table 16. The ENDF/B-VI values for k_{∞} for the unrodded and rodged bundles at BoL are statistically identical to the corresponding ENDF/B-V values. However, the ENDF/B-VI value for the depleted bundle is slightly but significantly lower than the ENDF/B-V value. At a uranium burnup of 25 MW·d/kg, ^{235}U accounts for less than 50% of the fissions in this bundle, and sensitivity studies demonstrated that the small reduction in reactivity is attributable primarily to differences between the evaluations for ^{238}U . At BoL, the differences between the ^{235}U cross-section libraries compensate for the differences between the ^{238}U libraries, but at 25 MW·d/kg the reduced ^{235}U content cannot completely offset the effects of the ^{238}U differences. The sensitivity studies also demonstrated that differences between the ENDF/B-V and ENDF/B-VI evaluations for the plutonium isotopes do not produce a significant reactivity change for the depleted bundle.

Table 16. Results for BWR fuel bundles.

Case title	k_{∞} , ENDF/B-VI	k_{∞} , ENDF/B-V	$\Delta\rho$
BWR bundle, unrodded	1.1292 ± 0.0007	1.1293 ± 0.0006	-0.0001 ± 0.0007
BWR bundle, rodged	0.9603 ± 0.0007	0.9595 ± 0.0006	0.0009 ± 0.0010
BWR bundle, depleted	0.9726 ± 0.0005	0.9746 ± 0.0005	-0.0021 ± 0.0007

RBMK Lattice

The idealized RBMK lattice corresponds to an infinite lattice of fuel cells for an RBMK reactor at BoL.⁵⁷ The central region contains 18 UO_2 fuel pins with an enrichment of 2.4 wt.%. The fuel pins are clad in stainless steel. The assembly is cooled by water flowing through the central tube in the lattice, and it is moderated by the surrounding block of graphite. The geometry of the fuel cell is shown in Figure 6.

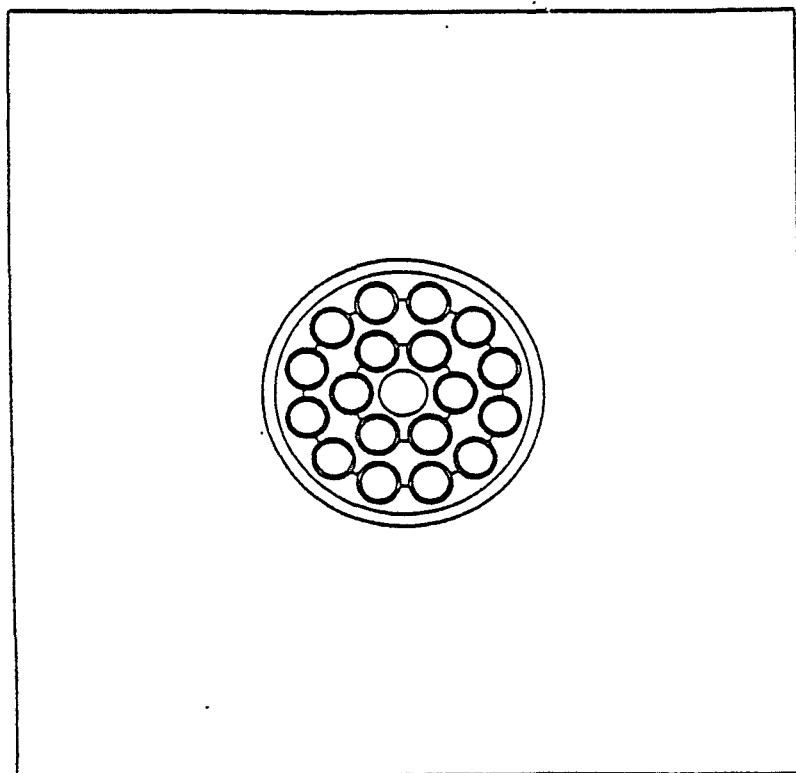


Figure 6. RBMK fuel cell.

Results for the RBMK fuel cell are summarized in Table 17. The ENDF/B-VI value for k_{∞} is only slightly lower than the ENDF/B-V value, but the difference is statistically significant. The reactivity difference is about the same as that observed for the OFA UO_2 pin cell with the same enrichment. Sensitivity studies indicated that, once again, the difference is due to competing effects from ^{235}U and ^{238}U .

Table 17. Results for RBMK lattice.

Case title	k_{∞} ENDF/B-VI	k_{∞} ENDF/B-V	$\Delta\rho$
RBMK fuel cell	1.3774 ± 0.0004	1.3750 ± 0.0004	-0.0013 ± 0.0006

MHTGR Lattice

The MHTGR lattice corresponds to an infinite array of standard core blocks for the MHTGR design that was developed as part of the now-discontinued New Production Reactor program.⁵⁸ Small spheres of HEU are contained in blocks of graphite moderator and are cooled by helium gas that flows through small channels bored in the graphite. A diagram of this standard cell block is shown in Figure 7.

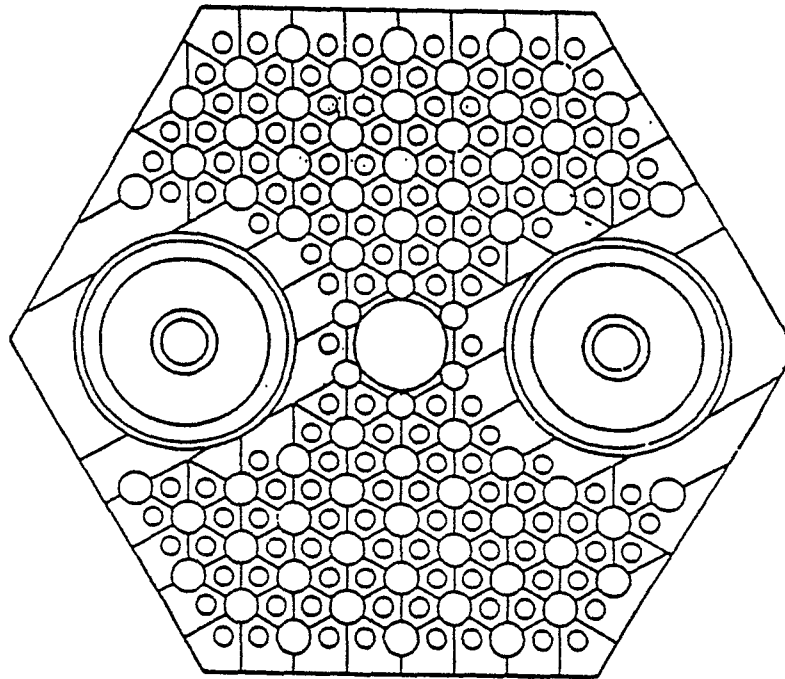


Figure 7. MHTGR standard core block.

Results for the MHTGR lattice are presented in Table 18. ENDF/B-VI produces a value for k_{∞} that is significantly higher than the ENDF/B-V value. Sensitivity studies demonstrated that this reactivity difference is due primarily to differences between the evaluations for ^{235}U . For the LEU cases discussed previously, differences between the ^{238}U evaluations tended to compensate for the differences between the ^{235}U evaluations. Such compensation does not occur here, however, because the fuel is highly enriched.

Table 18. Results for MHTGR lattice.

Case title	k_{∞} ENDF/B-VI	k_{∞} ENDF/B-V	$\Delta\rho$
MHTGR cell	1.1367 ± 0.0009	1.1317 ± 0.0010	0.0039 ± 0.0013

CANDU Cluster

The CANDU cluster contains 37 fuel pins surrounded by a heavy-water coolant and a heavy-water moderator. The pins contain natural uranium in the form of UO_2 , and they are clad in a zirconium alloy. The outer radius of the fuel is 0.25 cm, and the cladding is 0.15 cm thick. As Figure 8 illustrates, the fuel is arranged in rings of 1, 6, 12, and 18 pins. The fuel pins and their surrounding coolant are contained inside a zirconium-alloy pressure tube, which in turn is contained inside a zirconium-alloy calandria tube. The calandria tube is surrounded by the heavy-water moderator. This case is based on the "sample cluster case" from WIMS-AECL user's manual.⁵⁹

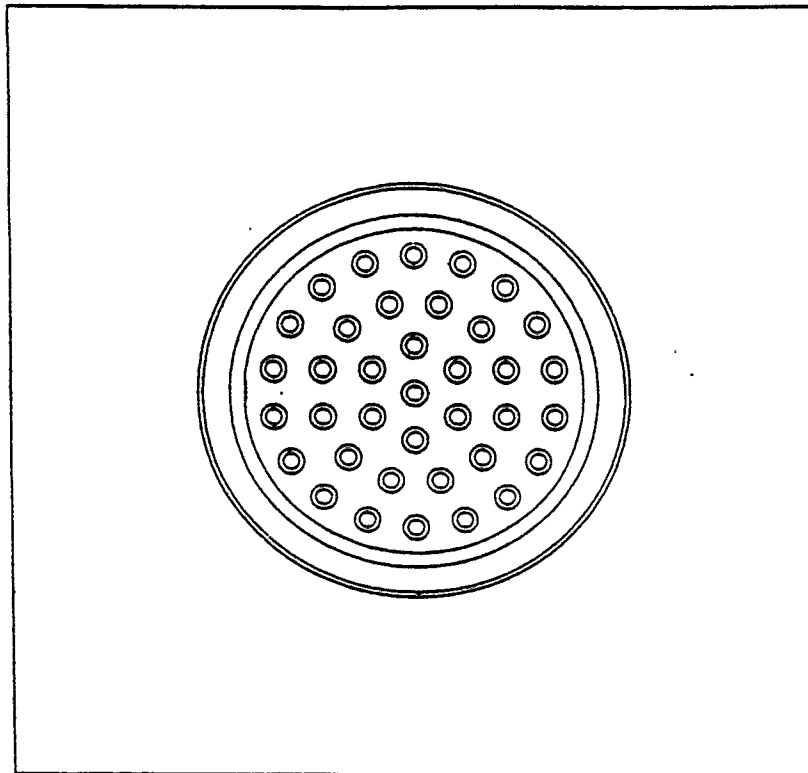


Figure 8. CANDU cluster.

The results for the CANDU cluster are summarized in Table 19. The ENDF/B-VI value for k_{∞} is slightly but significantly lower than the ENDF/B-V value. Although this pattern is consistent with that previously seen for PWR UO_2 lattices, its cause is not entirely the same. The reduction in reactivity is due almost entirely to differences between the ENDF/B-V and ENDF/B-VI cross sections for ^{16}O and for ^{238}U ; the reactivity effect of the cross-section differences for ^{235}U is negligible. The reactivity change due to ^{16}O is approximately the same as the reactivity change due to ^{238}U . Although reactivity changes due to ^{16}O were observed previously for critical experiments with significant neutron leakage (including one with heavy water), there is no leakage for the CANDU cluster because it is represented as an infinite lattice. The neutron capture by oxygen is about 20% higher in the ENDF/B-VI calculation than in the ENDF/B-V calculation, but oxygen is such a weak absorber that the increase in capture accounts for less than half of the observed reactivity difference. Consequently, the remainder of that difference is presumed to result

from changes in the capture rate of other isotopes due to spectral changes induced by differences between the ENDF/B-V and ENDF/B-VI evaluations for ^{16}O .

Table 19. Results for CANDU lattice.

Case title	k_{∞} ENDF/B-VI	k_{∞} ENDF/B-V	$\Delta\rho$
CANDU cluster	1.0036 ± 0.0003	1.0069 ± 0.0003	-0.0043 ± 0.0004

HWPR Cell and Supercell

These cases mimic the hexagonal fuel cell and the repeating lattice of supercells that formed the Mark 22 design for the Savannah River K-Reactor.⁶⁰ Inside a fuel assembly, rings of HEU are surrounded by flow channels for the heavy-water coolant and by rings of absorber material containing boron. The heavy water that is external to the fuel assembly acts as the moderator. Six hexagonal fuel cells and the hexagonal control cell that they surround form a supercell. The geometry of the supercell is shown in Figure 9.

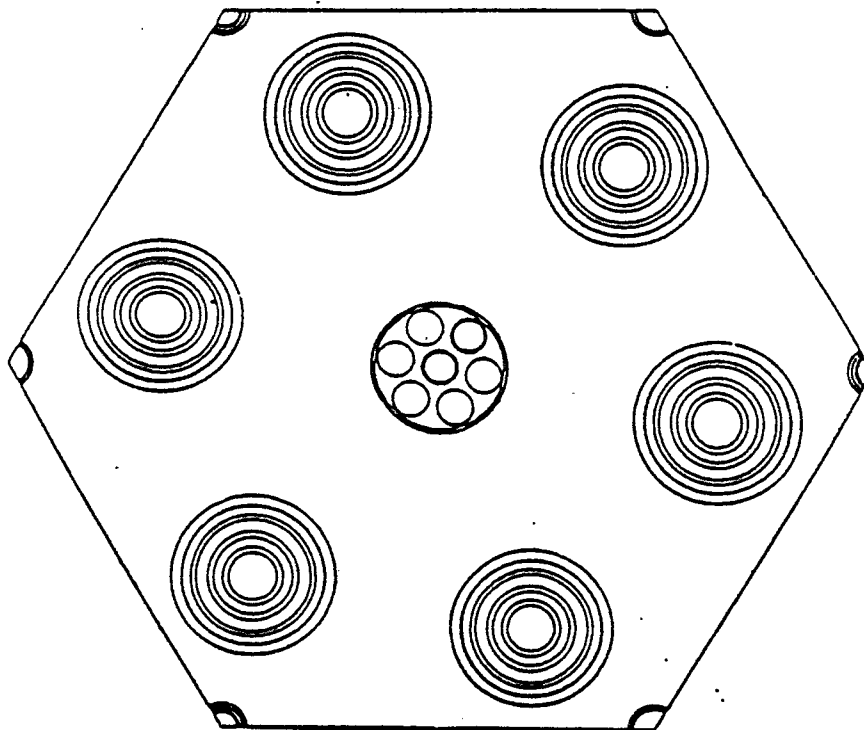


Figure 9. HWPR supercell.

Results from calculations for the HWPR cell and supercell are presented in Table 20. The ENDF/B-VI values for k_{∞} are only marginally higher than their ENDF/B-V counterparts, even though the uranium is HEU. However, the coolant and moderator are

heavy water. The differences between the ENDF/B-VI and ENDF/B-V evaluations for ^{235}U do produce a small increase in reactivity, but the differences between the ^{16}O evaluations tend to compensate for it. Consequently, the patterns observed previously for HEU fuel and for heavy water continue to hold, but they largely offset each other.

Table 20. Results for HWPR cell and supercell.

Case title	k_{eff} ENDF/B-VI	k_{eff} ENDF/B-V	$\Delta\rho$
Modified Mark 22 cell	1.0655 ± 0.0009	1.0641 ± 0.0009	0.0012 ± 0.0011
Modified Mark 22 supercell	0.9113 ± 0.0008	0.9129 ± 0.0008	0.0019 ± 0.0014

EFFECT OF ENDF/B-VI RELEASE 3 FOR ^{235}U

As was noted previously, the ENDF/B-VI continuous-energy libraries for MCNP were generated from the evaluations that were current through ENDF/B-VI.2. However, ENDF/B-VI.3 included an updated evaluation⁶¹ for ^{235}U . The revisions to that evaluation are limited to the energy range below 900 eV and principally affect the range below 110 eV.^{62,63} The changes increase the capture resonance integral and slightly reduce the fission resonance integral. This combination increases the epithermal capture-to-fission ratio and thereby improves the agreement of that parameter with measured values. Thermal data also were revised slightly to increase reactivity and thereby to partially offset the epithermal reduction in reactivity.

"Unthinned" continuous-energy libraries for ^{235}U were generated at LANL based on the ENDF/B-VI.2 and ENDF/B-VI.3 evaluations so that the effects of differences between the revisions could be investigated without being masked by approximations introduced during the processing of those evaluations into cross-section libraries. The unthinned libraries are several times larger than the libraries normally employed because, as the term suggests, they employ a much finer energy grid. Consequently, they constitute a more rigorous representation of the evaluation because approximations that are introduced during processing are minimized.

The calculations for the critical-experiment benchmarks with bare spheres of HEU uranyl nitrate and with lattices of UO_2 fuel pins were repeated with the unthinned ENDF/B-VI.2 and ENDF/B-VI.3 libraries. The values obtained for k_{eff} are compared to those obtained previously in Tables 21 and 22.

Table 21. k_{eff} for ORNL spheres.

Case	ENDF/B-V	ENDF/B-VI.2, thinned	ENDF/B-VI.2, unthinned	ENDF/B-VI.3, unthinned
ORNL-1	1.0005 ± 0.0006	0.9951 ± 0.0005	0.9961 ± 0.0006	0.9972 ± 0.0006
ORNL-2	0.9981 ± 0.0006	0.9968 ± 0.0006	0.9939 ± 0.0006	0.9973 ± 0.0006
ORNL-3	0.9961 ± 0.0006	0.9943 ± 0.0006	0.9935 ± 0.0006	0.9945 ± 0.0006
ORNL-4	0.9964 ± 0.0006	0.9939 ± 0.0006	0.9944 ± 0.0007	0.9943 ± 0.0006
ORNL-10	0.9996 ± 0.0004	0.9972 ± 0.0004	0.9959 ± 0.0004	0.9975 ± 0.0004

Table 22. k_{eff} for B&W core XI benchmarks.

Loading	ENDF/B-V	ENDF/B-VI.2, thinned	ENDF/B-VI.2, unthinned	ENDF/B-VI.3, unthinned
1	0.9981 ± 0.0003	0.9963 ± 0.0003	0.9957 ± 0.0003	0.9956 ± 0.0003
2	0.9988 ± 0.0003	0.9964 ± 0.0003	0.9965 ± 0.0003	0.9957 ± 0.0003
8	0.9965 ± 0.0003	0.9944 ± 0.0003	0.9945 ± 0.0003	0.9940 ± 0.0003

These results suggest that the reactivity differences between the thinned and unthinned ENDF/B-VI.2 libraries are negligible for the lattices. However, the results for the ORNL spheres demonstrate that differences in the processing of the thinned and unthinned libraries can produce effects that are comparable in magnitude to those caused by differences in the ENDF/B-VI.2 and ENDF/B-VI.3 evaluations. Consequently, comparisons between those two evaluations hereafter will be based exclusively on the unthinned ENDF/B-VI.2 library. The ENDF/B-V results will continue to be based on a thinned ^{235}U library, however, because an unthinned ^{235}U library for MCNP was not available.

These results also suggest that the reactivity changes produced by ENDF/B-VI.3 are likely to be small. For that reason, the scope of the comparisons will be extended to include spectral indices as well as k_{eff} . These spectral indices are δ_{25} , δ_{28} , ρ_{25} , ρ_{28} , and the conversion ratio (CR). δ_{25} is the ratio of fast fissions to thermal fissions in ^{235}U , while δ_{28} is the ratio of fissions in ^{238}U to fissions in ^{235}U (summed over all energies). Similarly, ρ_{25} is the ratio of fast to thermal captures in ^{235}U , while ρ_{28} is the ratio of fast to thermal captures in ^{238}U . By convention, the breakpoint between the fast and thermal ranges is taken to be 0.625 eV. CR is the ratio of the production of fissile isotopes to the destruction of fissile isotopes; in the systems examined here, it is simply the ratio of captures in ^{238}U to absorptions in ^{235}U . Because all the cases studied employed 1,000,000 active neutron histories, the computed uncertainties in the spectral indices typically are less than 1% (and often substantially so.) Consequently, those uncertainties will be ignored in the discussion that follows.

Lattices

Comparisons were made for six different lattices with UO_2 fuel: NB-1, NB-5, the OFA PWR cell with 1.6 wt% enrichment, the standard PWR cell with 3.9 wt% enrichment, the CANDU cluster, and the RBMK fuel cell. The first four lattices are moderated by light water, while the other two are moderated by heavy water and by graphite, respectively.

As was noted earlier, NB-1 has a low enrichment (1.3 wt%) and a relatively soft spectrum. The results for NB-1 are shown in Table 23. The ENDF/B-VI.3 result for ρ_{25} increases by nearly 8% relative to that for ENDF/B-VI.2 (and by more than 3% relative to ENDF/B-V). The increase in epithermal ^{235}U capture reduces k_{eff} slightly, but it has relatively little impact on the other spectral indices. With the notable exception of ρ_{25} , the results from ENDF/B-VI.3 tend to accentuate the differences between ENDF/B-V and ENDF/B-VI rather than to reduce them.

NB-5 has a very tight lattice and consequently a relatively hard spectrum, as a comparison of values from Table 24 with those from Table 23 demonstrates. Because the largest differences between the ENDF/B-VI.2 and ENDF/B-VI.3 evaluations occur in the epithermal range, the harder spectrum in NB-5 produces larger differences between the spectral indices than occurred for NB-1. ρ_{25} still increases by essentially the same amount (nearly 8%), but because of the harder spectrum the increase in epithermal ^{235}U capture has

Table 23. Results for NB-1.

Library	k_{∞}	δ_{25}	δ_{28}	ρ_{25}	ρ_{28}	CR
ENDF/B-V	1.1435 ± 0.0005	0.08259	0.07234	0.2206	1.387	0.6739
ENDF/B-VI.2	1.1400 ± 0.0005	0.08155	0.07240	0.2116	1.398	0.6795
ENDF/B-VI.3	1.1384 ± 0.0005	0.08108	0.07240	0.2280	1.401	0.6792

a larger impact on k_{∞} , which decreases by $0.0044 \pm 0.0007 \Delta\rho$ relative to ENDF/B-VI.2. Furthermore, the difference between the ENDF/B-VI.3 and ENDF/B-V values for ρ_{25} is more than 6%, which is double the difference for NB-1. In addition, the further hardening of the spectrum from the increase in epithermal ^{235}U capture increases not only δ_{25} but also δ_{28} and ρ_{28} (at least marginally). The increased capture in ^{235}U more than compensates for the increased capture in ^{238}U from the hardening of the spectrum, and therefore CR decreases.

Table 24. Results for NB-5.

Library	k_{∞}	δ_{25}	δ_{28}	ρ_{25}	ρ_{28}	CR
ENDF/B-V	1.1376 ± 0.0006	0.5547	0.1347	1.378	8.725	0.8051
ENDF/B-VI.2	1.1392 ± 0.0006	0.5491	0.1357	1.357	8.734	0.8155
ENDF/B-VI.3	1.1335 ± 0.0006	0.5555	0.1360	1.464	8.735	0.8095

The results for the OFA pin cell with an enrichment of 1.6 wt.% are shown in Table 25. The pattern of those results is very similar to that for NB-1. The only parameter that changes substantially from ENDF/B-VI.2 to ENDF/B-VI.3 is ρ_{25} , which again increases by nearly 8%. To the extent that the other parameters do change, they tend to accentuate the differences between ENDF/B-VI and ENDF/B-V rather than to mitigate them. The similarity between the results from NB-1 and this case is not surprising, because both of them contain slightly enriched fuel and have a relatively soft spectrum.

Table 25. Results for OFA pin cell with 1.6 wt.% enrichment.

Library	k_{∞}	δ_{25}	δ_{28}	ρ_{25}	ρ_{28}	CR
ENDF/B-V	0.9160 ± 0.0005	0.09821	0.07258	0.2627	1.762	0.6284
ENDF/B-VI.2	0.9144 ± 0.0005	0.09687	0.07275	0.2523	1.771	0.6334
ENDF/B-VI.3	0.9137 ± 0.0005	0.09639	0.07273	0.2725	1.775	0.6328

The results for the standard PWR pin cell with an enrichment of 3.9 wt.% are shown in Table 26. Those results are intermediate between those for the OFA cell and NB-5. This behavior is not surprising, because the spectrum for this case is intermediate between the relatively hard spectrum of NB-5 and the relatively soft spectrum of the OFA cell. Once again, the ENDF/B-VI.3 value for ρ_{25} is nearly 8% higher than the ENDF/B-VI.2 value, and the reactivity decreases (although by an intermediate amount, $0.0016 \pm 0.0005 \Delta\rho$). The changes in the other spectral indices are quite small.

Table 26. Results for standard pin cell with 3.9 wt.% enrichment.

Library	k_{∞}	δ_{25}	δ_{28}	ρ_{25}	ρ_{28}	CR
ENDF/B-V	1.2468 ± 0.0006	0.1959	0.05648	0.5059	3.532	0.3806
ENDF/B-VI.2	1.2484 ± 0.0006	0.1932	0.05647	0.4917	3.562	0.3859
ENDF/B-VI.3	1.2459 ± 0.0006	0.1922	0.05677	0.5312	3.563	0.3845

The ENDF/B-VI.3 value for ρ_{25} for the CANDU cluster also increases by nearly 8% relative to the corresponding ENDF/B-VI.2 value, but, as shown in Table 27, the spectrum for that case is so soft that it has very little impact on k_{∞} or the other spectral indices. (For example, the CANDU value for ρ_{28} is only about 40% as large as that for NB-1, which has the softest spectra of any of the previous four cases.) However, it is noteworthy that, even for this case, the ENDF/B-VI.3 changes to the thermal data for ^{235}U produce only a marginal increase in reactivity.

Table 27. Results for CANDU fuel cluster.

Library	k_{∞}	δ_{25}	δ_{28}	ρ_{25}	ρ_{28}	CR
ENDF/B-V	1.0079 ± 0.0003	0.007988	0.008371	0.02770	0.8723	1.0472
ENDF/B-VI.2	1.0035 ± 0.0003	0.007959	0.008431	0.02177	0.8950	1.0695
ENDF/B-VI.3	1.0041 ± 0.0003	0.007904	0.008440	0.02346	0.8876	1.0565

The RBMK fuel cell also produces a very thermal spectrum, although it is slightly harder than that for the CANDU cluster. As Table 28 demonstrates, the patterns for the CANDU cluster also characterize the RBMK cell. Although ρ_{25} increases by slightly more than 8% for this case, it has only marginal impact on k_{∞} and the other spectral indices.

Table 28. Results for RBMK fuel cell.

Library	k_{∞}	δ_{25}	δ_{28}	ρ_{25}	ρ_{28}	CR
ENDF/B-V	1.3774 ± 0.0004	0.05569	0.02405	0.1496	0.9467	0.3048
ENDF/B-VI.2	1.3754 ± 0.0004	0.05465	0.02419	0.1428	0.9520	0.3067
ENDF/B-VI.3	1.3748 ± 0.0004	0.05469	0.02423	0.1546	0.9565	0.3069

Solutions

Comparisons were made for four different solutions, two with HEU uranyl nitrate (ORNL-4 and ORNL-10), one with LEU uranyl fluoride (SHEBA-II), and one with HEU uranyl fluoride (sphere of uranyl fluoride in heavy water).

ORNL-4 has the hardest spectrum of any of the ORNL HEU uranium-nitrate spheres because it contains the most boron and has the highest concentration of fissile material. Nonetheless, its spectrum is more thermal than that of any of the lattices discussed above except the CANDU cluster. As Table 29 illustrates, the value of ρ_{25} increases by slightly less than 8% for ENDF/B-VI.3 relative to ENDF/B-VI.2, but the changes in δ_{25} , δ_{28} , and k_{∞} are essentially negligible. The reduction in ρ_{28} most likely is due to competition

between ^{235}U and ^{238}U rather than to a spectral effect, because the increase in ^{235}U epithermal capture should harden the spectrum rather than soften it. Similarly, the reduction in CR is due primarily to the small overall increase in ^{235}U absorption.

Table 29. Results for ORNL-4.

Library	k_{∞}	δ_{25}	δ_{28}	ρ_{25}	ρ_{28}	CR
ENDF/B-V	0.9964 ± 0.0006	0.03044	2.505×10^{-5}	0.08670	6.112	1.646×10^{-3}
ENDF/B-VI.2	0.9944 ± 0.0007	0.02978	2.500×10^{-5}	0.08310	6.168	1.663×10^{-3}
ENDF/B-VI.3	0.9943 ± 0.0006	0.02990	2.497×10^{-5}	0.08954	6.025	1.628×10^{-3}

ORNL-10 has the softest spectrum of any of the ORNL HEU uranyl-nitrate spheres because it has the lowest leakage, contains no boron, and has the most dilute concentration of fissile material. Its spectrum is sufficiently thermal that ENDF/B-VI.3 predicts an increase in reactivity relative to ENDF/B-VI.2, even though its value for ρ_{25} is nearly 8% higher. This pattern is expected because of the differences between the ENDF/B-VI.3 and ENDF/B-VI.2 evaluations for ^{235}U in the deep thermal range. As shown in Table 30, the changes in the other spectral indices are essentially negligible.

Table 30. Results for ORNL-10.

Library	k_{∞}	δ_{25}	δ_{28}	ρ_{25}	ρ_{28}	CR
ENDF/B-V	0.9996 ± 0.0004	0.01759	1.344×10^{-5}	0.05041	3.588	1.010×10^{-3}
ENDF/B-VI.2	0.9959 ± 0.0004	0.01740	1.336×10^{-5}	0.04814	3.553	1.004×10^{-3}
ENDF/B-VI.3	0.9975 ± 0.0004	0.01730	1.335×10^{-5}	0.05182	3.562	1.005×10^{-3}

SHEBA-II has a harder spectrum than any of the ORNL HEU spheres, because its leakage is higher and, even though it contains LEU rather than HEU, its concentration of fissile material is nearly double that of the ORNL sphere with the highest fissile concentration. Nonetheless, its overall spectrum is intermediate between those of the lattice cases (softer than NB-5 and the 3.9 wt.% pin cell but harder than the others). As the results in Table 31 illustrate, the ENDF/B-VI.3 value for k_{∞} is marginally higher than that for ENDF/B-VI.2, even though the ENDF/B-VI.3 value for ρ_{25} is approximately 8% higher than its ENDF/B-VI.2 counterpart. The small decrease in δ_{25} probably is due to increased competition for epithermal neutrons between capture and fission. The differences between the ENDF/B-VI.3 and ENDF/B-VI.2 results for δ_{28} , ρ_{28} , and CR are negligible.

Table 31. Results for SHEBA-II.

Library	k_{∞}	δ_{25}	δ_{28}	ρ_{25}	ρ_{28}	CR
ENDF/B-V	1.0115 ± 0.0008	0.05772	0.01524	0.1604	2.578	0.2623
ENDF/B-VI.2	1.0063 ± 0.0008	0.05681	0.01525	0.1531	2.593	0.2644
ENDF/B-VI.3	1.0077 ± 0.0008	0.05540	0.01529	0.1657	2.596	0.2641

The reflected sphere of uranyl fluoride in heavy water has the hardest spectrum of any of the solutions studied because it contains HEU, is moderated and reflected by heavy water, and has the highest leakage of any of the uranium solution experiments. Consequently, the differences in the results from ENDF/B-VI.3 and ENDF/B-VI.2 are more pronounced than for the other solutions, as Table 32 demonstrates. ρ_{25} increases by nearly 10%, and k_{eff} drops by more than 0.006 Δk . The effects on the other spectral indices also are more pronounced than in previous cases, although the actual changes remain relatively small. CR decreases by approximately 1.5% percent, and δ_{25} , δ_{28} , and ρ_{28} each change by between 0.5% and 1%. The small changes to these spectral indices most likely reflect increased competition between ^{235}U and ^{238}U for epithermal neutrons rather than a softening of the spectrum.

Table 32. Results for reflected sphere of uranyl fluoride in heavy water.

Library	k_{eff}	δ_{25}	δ_{28}	ρ_{25}	ρ_{28}	CR
ENDF/B-V	0.9967 ± 0.0010	0.3962	8.461×10^{-5}	1.097	68.93	0.01143
ENDF/B-VI.2	1.0048 ± 0.0010	0.3884	8.416×10^{-5}	1.055	69.46	0.01167
ENDF/B-VI.3	0.9984 ± 0.0010	0.3858	8.473×10^{-5}	1.160	68.88	0.01149

Overall, the reactivity differences between ENDF/B-VI.2 and ENDF/B-VI.3 are essentially negligible for most of these lattices and solutions. However, as the results for NB-5 and the sphere of uranyl fluoride in heavy water demonstrate, ENDF/B-VI.3 does produce a lower reactivity than ENDF/B-VI.2 for the cases with harder spectra.

DATA TESTING: TIME-OF-FLIGHT MEASUREMENTS

LLNL Pulsed-Sphere Experiments

The pulsed-sphere benchmark experiments were performed at Lawrence Livermore National Laboratory (LLNL) beginning in the 1960s and continuing through the 1980s.⁶⁴⁻⁶⁹ The primary purpose of these benchmark experiments was to address the need for detailed neutron transport measurements that were sufficiently simple to calculate, yet complex enough to test some of the more sophisticated features of the transport codes and cross-section data.

These experiments used an almost isotropic 14-MeV neutron source created at the center of a sphere of target material from the $d(t,n)^4\text{He}$ reaction at 400 keV. The neutron emission spectrum was measured using time-of-flight techniques over an energy range from 10 eV to 14 MeV. For the low-energy data between 10 eV and 1 MeV, a ^6Li -loaded glass scintillator was used, while a Pilot B or NE213 scintillator was used for the high-energy measurements from 2 to 15 MeV. These detectors were placed at angles of 26°, 30°, and 120° with respect to the incident d-beam direction, and they had flight paths ranging from 750 to 975 cm. A representative experimental setup is shown in Figure 10.

The thickness of the target materials ranged from 0.5 to 5.0 mean free paths (mfp) for the 14-MeV neutrons. The target materials included nuclides from ^1H to ^{239}Pu , as well as composite materials such as concrete. Later experiments from the 1980s also included photon production measurements for the various targets. This discussion will focus on the high-energy range from the earlier neutron-transmission measurements.⁶⁶⁻⁶⁹ These earlier experiments included at least 49 measurements for 21 target materials. There were three

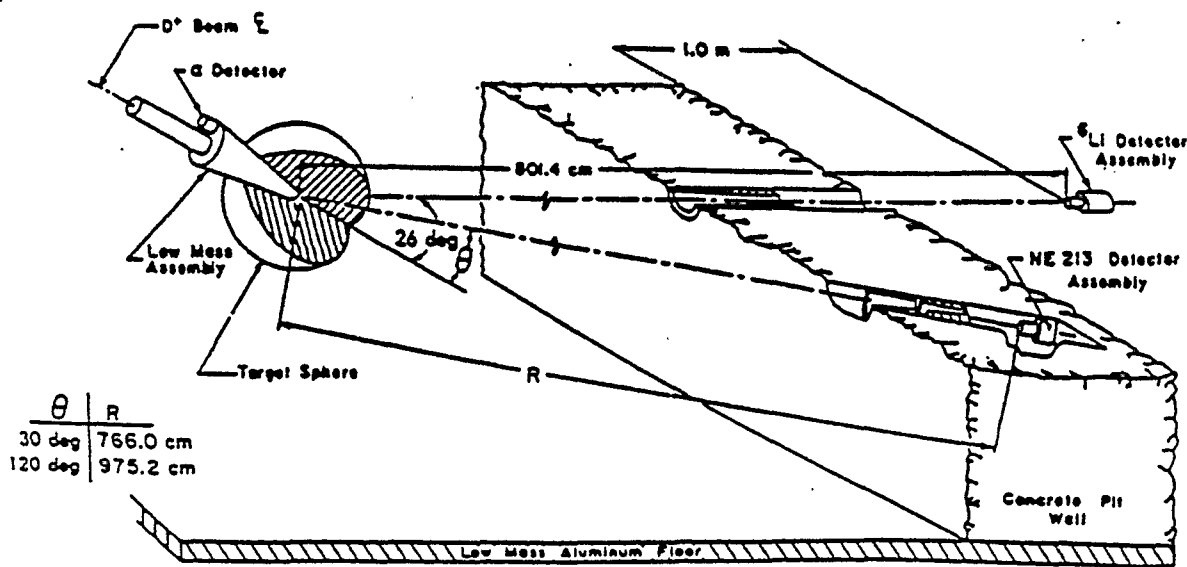


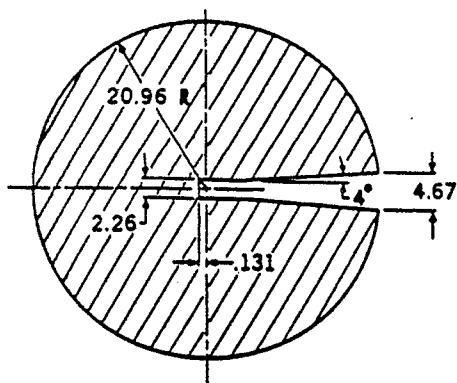
Figure 10. Experimental setup for the LLNL pulsed-sphere measurements.

types of target assemblies: (1) bare spheres of materials such as carbon, (2) clad spheres of materials such as the stainless-steel-clad lead sphere, and (3) spherical stainless-steel dewars for materials such as light water. Figures 11, 12, and 13 illustrate these spherical geometries for the 2.9 mfp carbon sphere, the 1.4 mfp lead sphere, and the 1.9 mfp light-water dewar, respectively. Region 1 in Figure 12 is lead, and region 2 is stainless steel; region 1 in Figure 13 contains water, while regions 2 and 3 are stainless steel. The measured data for each spherical assembly ("target in") was normalized to the total flux measured with the material of interest removed from the spherical assembly ("target out").

LLNL Pulsed-Sphere Benchmarks

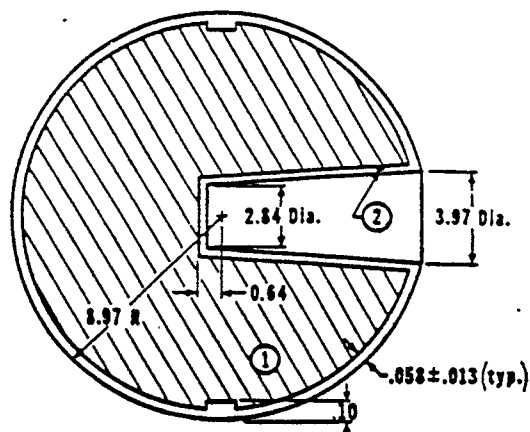
The high-energy pulsed-sphere benchmarks were first implemented for MCNP3B in the late 1970s⁷⁰ and later for MCNP4A.^{71,72} We recently made revisions to these earlier implementations of the benchmarks, as well as implementing benchmarks for additional materials. Currently, we have implemented 36 benchmarks for 20 target materials, including 17 nuclides and 5 composite materials (light and heavy water, polyethylene, teflon, and concrete) as indicated in Tables 33 and 34, respectively. With the exception of Mg, Al, Si, Ti and W, these nuclides represent new evaluations for ENDF/B-VI.

Revisions to the previously reported results^{71,72} include small geometry, source, and material corrections, improvements in the detector efficiencies used in the MCNP tallies, changes in some of the density specifications, and a more accurate conversion from time of flight to energy. In earlier implementations, the density was altered to reflect the total mass reported in various publications. In the revised benchmarks, densities reported in later publications were used for those materials.^{64,65} The improved relativistic conversion



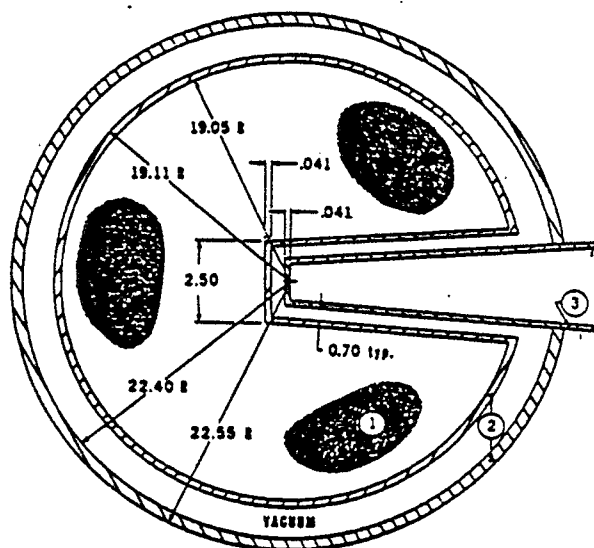
All dimensions are in cm.

Figure 11. Bare target assembly for 2.9 mfp carbon.



All dimensions are in cm.

Figure 12. Clad target assembly for 1.4 mfp lead.



All dimensions are in cm.

Figure 13. Dewar assembly for 1.9 mfp light water.

between the time of flight and the neutron energy is⁶⁶

$$E = 939.58 \left[\sqrt{\frac{1}{1 - \left(\frac{L}{ct}\right)^2}} - 1 \right] \quad (4)$$

where E is the energy in MeV, L is the flight path in cm, c is the speed of light, and t is the time in shakes (1 shake = 10 ns, so $c = 3 \times 10^{10}$ cm/sec = 300 cm/shake).

The source specification for the $d(t,n)^4\text{He}$ reaction includes the appropriate energy and angle distributions with respect to the incident d-beam direction, and it also includes the appropriate Gaussian time distribution for each experiment.^{67,70} For the lighter materials,

Table 33. Pulsed-sphere benchmarks for isotopes.

Material	Radius (mfp)	Flight path (cm)	Angle	Detector
⁶ Li	0.5	746.34	26°	NE213
	1.1	*	*	*
	1.6	746.34	26°	NE213
⁷ Li	0.5	746.34	26°	NE213
	1.0	*	*	*
	1.6	746.34	26°	NE213
Be	0.8	765.2	30°	Pilot B
C	0.5	766.0	30°	NE213
	1.3	*	*	*
	2.9	766.0	30°	NE213
N	1.1	763.3	30°	Pilot B
	3.1	765.2	30°	Pilot B
O	0.7	754.0	30°	Pilot B
Mg	0.7	765.2	30°	Pilot B
	1.2	*	*	*
	1.9	765.2	30°	Pilot B
Al	0.9	765.2	30°	Pilot B
	1.6	*	*	*
	2.6	765.2	30°	Pilot B
Ti	1.2	765.2	30°	Pilot B
	2.2	*	*	*
	3.5	765.2	30°	Pilot B
Fe	0.9	766.0	30°	NE213
	2.9	*	*	*
	4.8	766.0	30°	NE213
W	0.5	*	*	*
	0.9	801.4	26°	NE213
	1.7	*	*	*
	3.2	801.4	26°	NE213
Pb	1.4	766.0	30°	NE213
²³⁵ U	0.7	945.54	26°	NE213
	1.5	945.54	26°	NE213
²³⁸ U	0.8	945.54	26°	NE213
	2.8	746.34	26°	NE213
²³⁹ Pu	0.7	945.54	26°	NE213

* Not implemented.

Table 34. Pulsed-sphere benchmarks for composite materials.

Material	Radius (mfp)	Flight path (cm)	Angle	Detector
Light water (H ₂ O)	1.1	754.0	30°	Pilot B
	1.9	754.0	30°	Pilot B
Heavy water (D ₂ O)	1.2	765.2	30°	Pilot B
	2.1	765.2	30°	Pilot B
Polyethylene (CH ₂)	0.8	754.0	30°	Pilot B
	1.6	^a	^a	^a
	3.5	765.0	30°	Pilot B
Teflon (CF ₂)	0.9	765.2	30°	Pilot B
	1.8	^a	^a	^a
	2.9	765.2	30°	Pilot B
Concrete ^b	2.0	975.4	120°	NE213
	3.8	975.4	120°	NE213

^a Not implemented^b The concrete contains 55.7 wt.% O, 15.1 wt.% H, 14.9 wt.% Si, 3.6 wt.% Ca, 3.2 wt.% Al, 3.1 wt.% C, 1.8 wt.% Mg, 1.3 wt.% Na, and traces of K, Ti, Mn, and Fe.

the actual target assembly for the neutron source does not need to be included in the simulation. Ring detectors were used to calculate the flux at a given detector location. The corresponding detector efficiency was folded into the MCNP tally using the DE (detector energy) and DF (dose function) cards for the Pilot B and NE213 detectors.^{66,67,69} The detector tallies were binned in 2-ns time bins. Simulations were performed for both the target-in and target-out measurements. The target-in results were then normalized to the total flux of the target-out results for comparison to the reported experimental data. A more detailed description of these benchmarks will be reported at a later date.⁷³

The results may be compared graphically or by tabulating the integrated flux ratios within specified energy bins. Figures 14 through 49 graphically compare the experimental results with results calculated using MCNP and its continuous-energy ENDF/B-V and ENDF/B-VI libraries. The time scale employed for these Figures is shakes, where one shake is 10 ns. Table 35 presents the same comparisons over the neutron energy ranges of 2-3, 3-5, 5-10, 10-13, and 13-16 MeV. The standard deviations in the values shown in Table 35 are less than the number of significant figures given for those values. Consequently, the standard deviations will be ignored.

Pulsed-Sphere Benchmark Results

As these results demonstrate, there is good agreement with the measurements for the light and fissionable nuclides and for the composite materials. However, the agreement for the larger spheres of the heavier, non-fissionable nuclides is not as good. The ⁶Li results show an underestimate of the flux over the energy region between 7.3 and 11.6 MeV (160-200 ns) but an overestimate of the flux at lower energies. The results for ⁷Li are in much better agreement, particularly for the larger sphere.

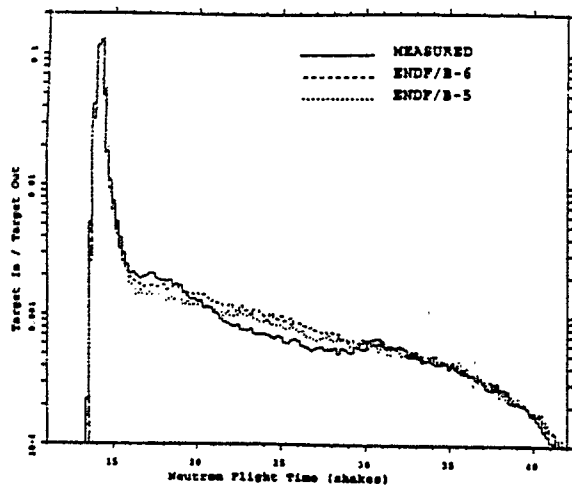


Figure 14. Normalized time-of-flight spectra for 0.5 mfp ${}^6\text{Li}$.

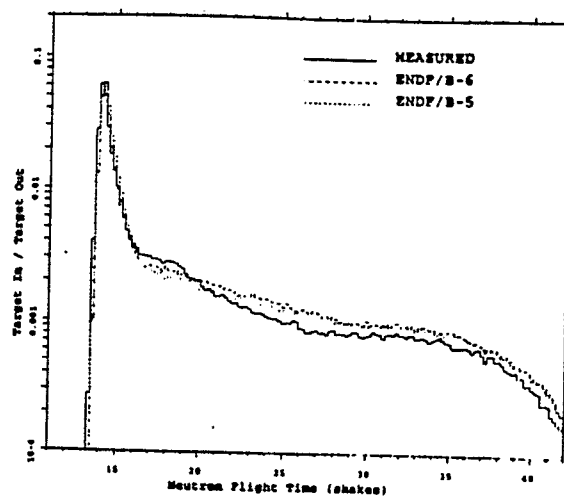


Figure 15. Normalized time-of-flight spectra for 1.6 mfp ${}^6\text{Li}$.

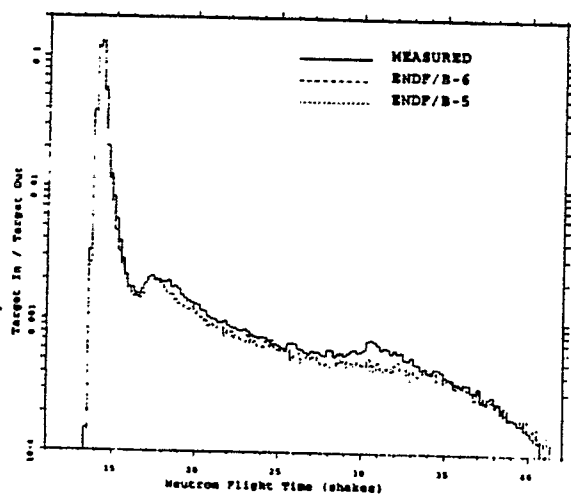


Figure 16. Normalized time-of-flight spectra for 0.5 mfp ${}^7\text{Li}$.

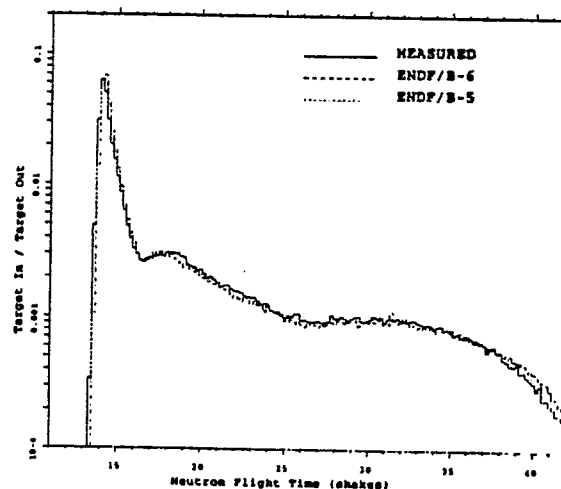


Figure 17. Normalized time-of-flight spectra for 1.6 mfp ${}^7\text{Li}$.

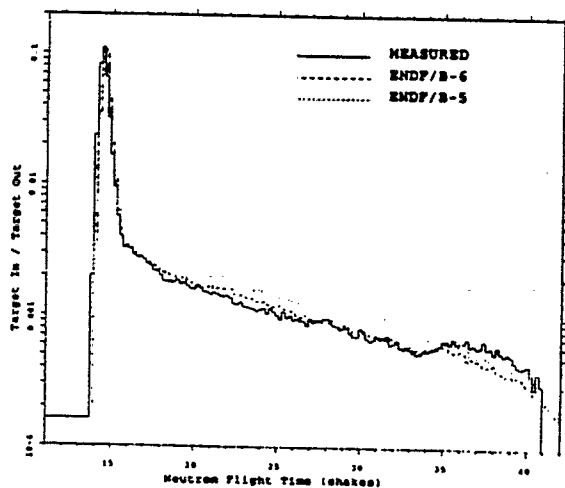


Figure 18. Normalized time-of-flight spectra for 0.8 mfp Be.

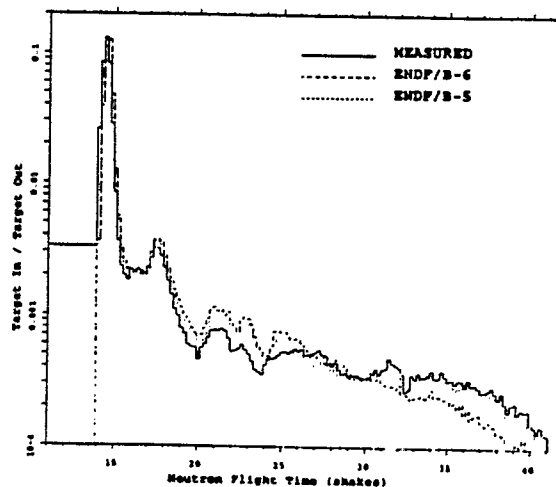


Figure 19. Normalized time-of-flight spectra for 0.5 mfp C.

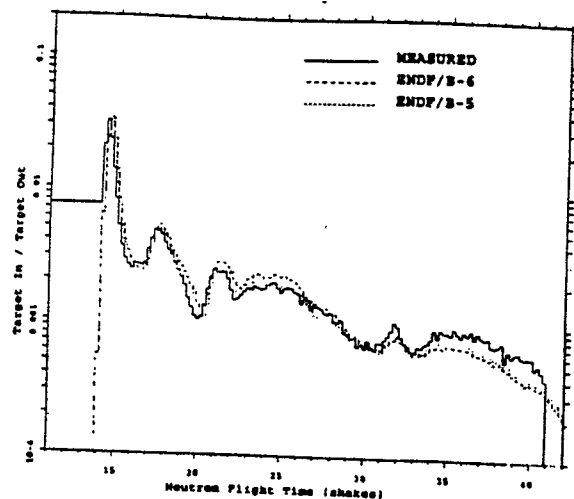


Figure 20. Normalized time-of-flight spectra for 2.9 mfp C.

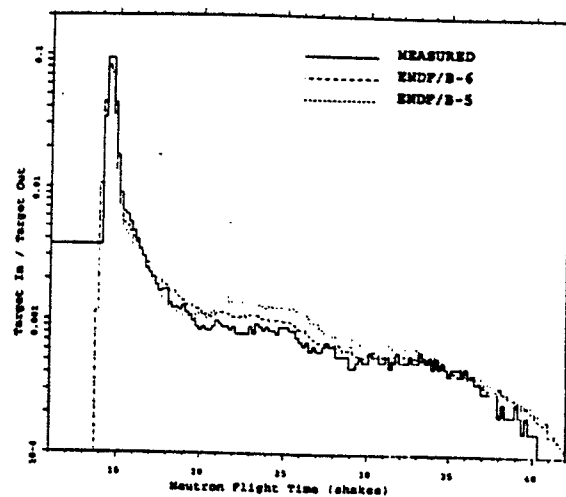


Figure 21. Normalized time-of-flight spectra for 1.1 mfp N.

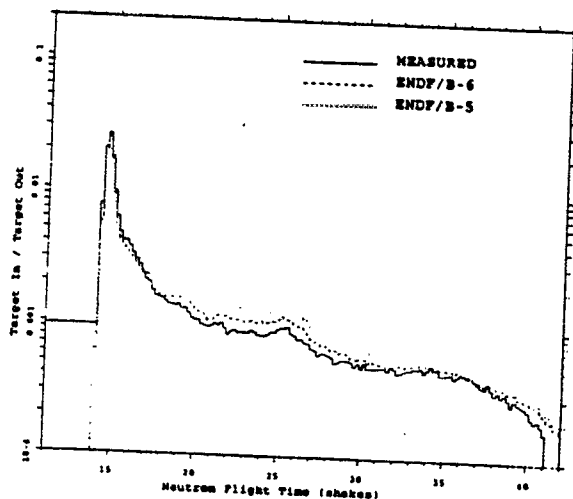


Figure 22. Normalized time-of-flight spectra for 3.1 mfp N.

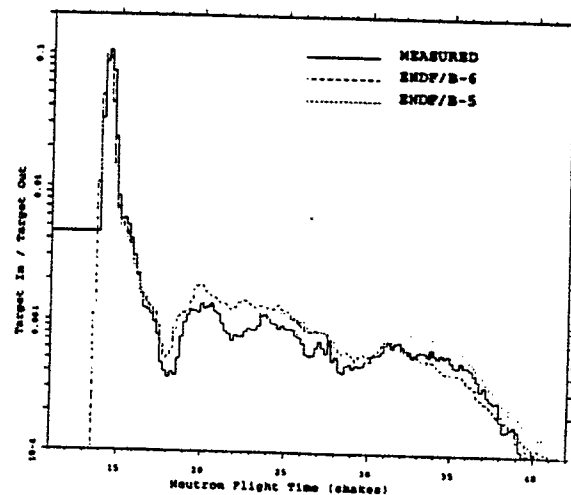


Figure 23. Normalized time-of-flight spectra for 0.7 mfp O.

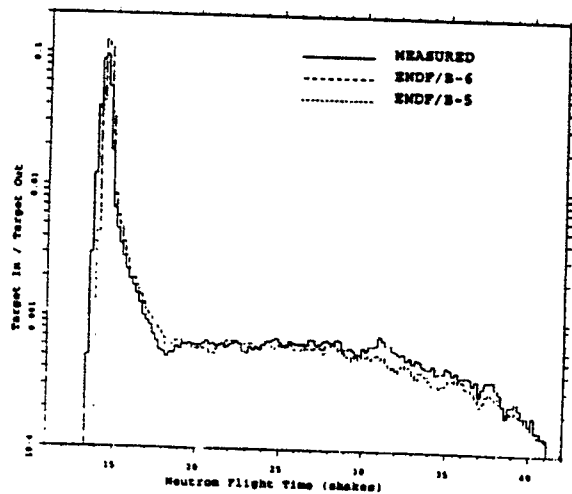


Figure 24. Normalized time-of-flight spectra for 0.7 mfp Mg.

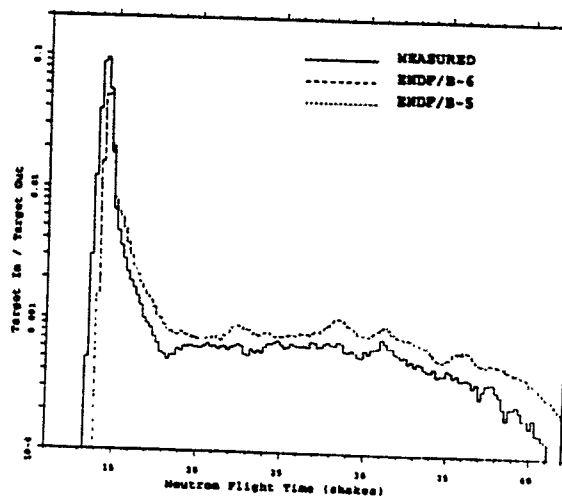


Figure 25. Normalized time-of-flight spectra for 1.9 mfp Mg.

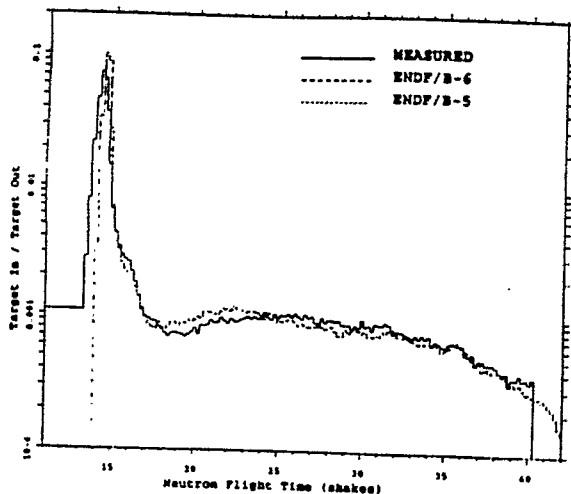


Figure 26. Normalized time-of-flight spectra for 0.9 mfp Al.

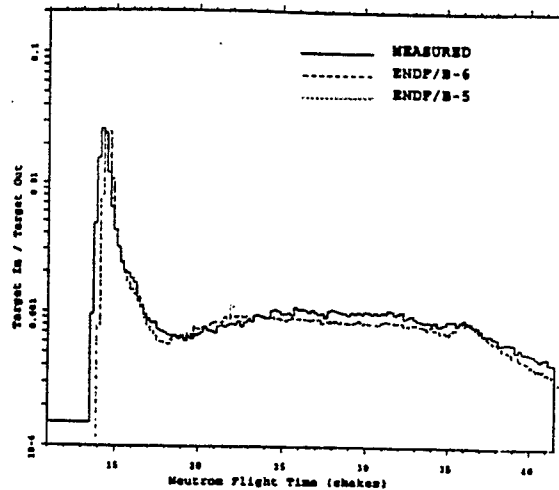


Figure 27. Normalized time-of-flight spectra for 2.6 mfp Al.

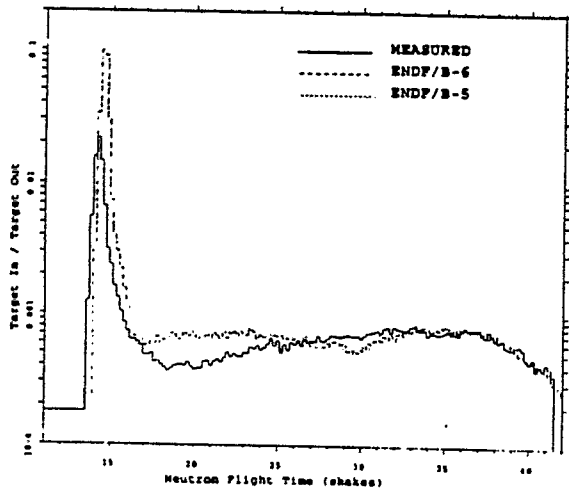


Figure 28. Normalized time-of-flight spectra for 1.2 mfp Ti.

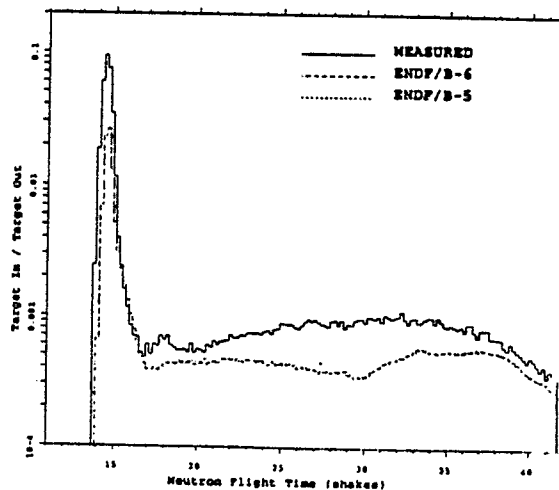


Figure 29. Normalized time-of-flight spectra for 3.5 mfp Ti.

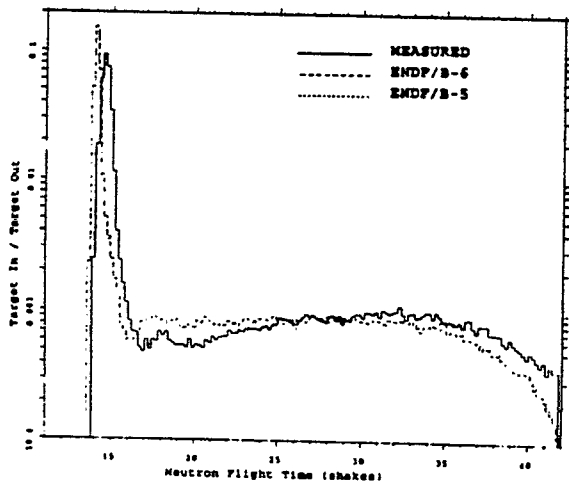


Figure 30. Normalized time-of-flight spectra for 0.9 mfp Fe.

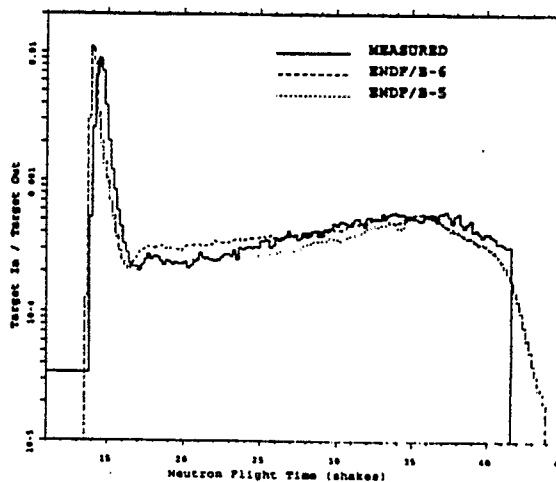


Figure 31. Normalized time-of-flight spectra for 4.8 mfp Fe.

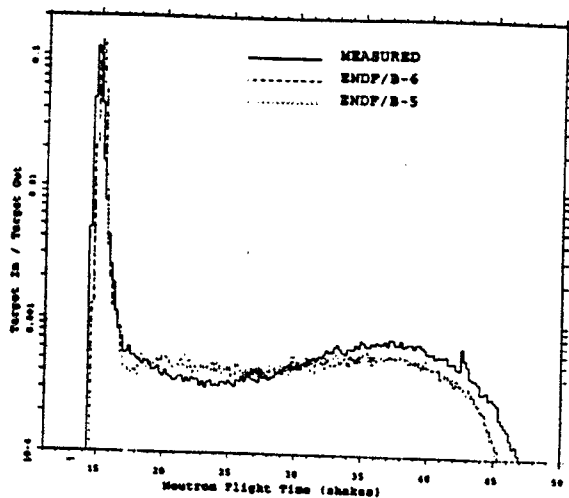


Figure 32. Normalized time-of-flight spectra for 0.9 mfp W.

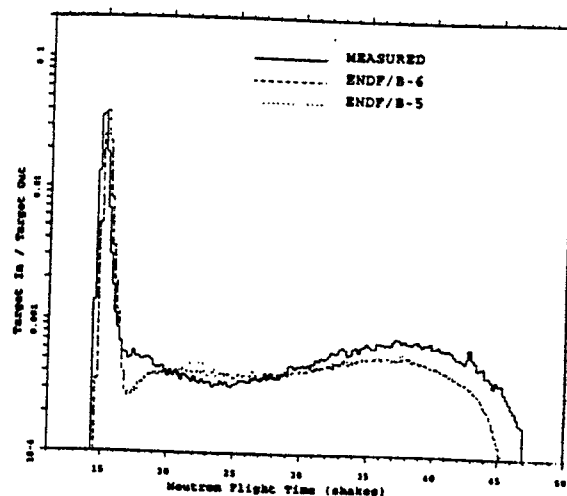


Figure 33. Normalized time-of-flight spectra for 3.2 mfp W.

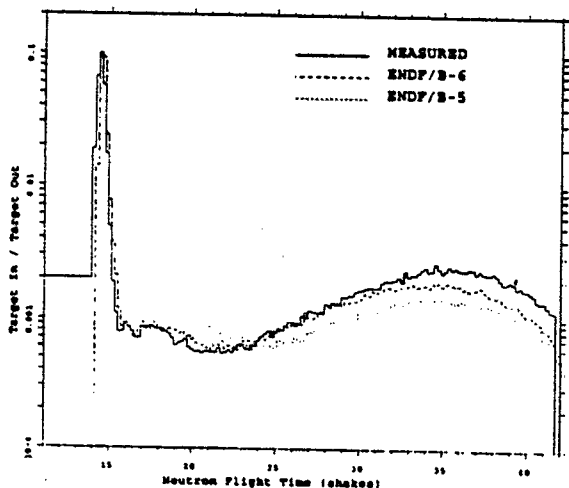


Figure 34. Normalized time-of-flight spectra for 1.4 mfp Pb.

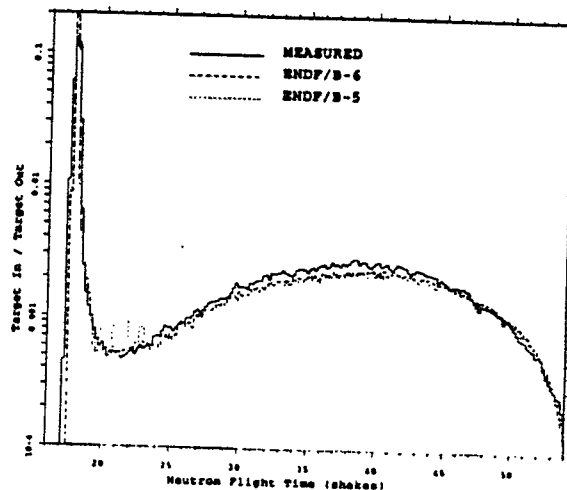


Figure 35. Normalized time-of-flight spectra 0.7 mfp ^{235}U .

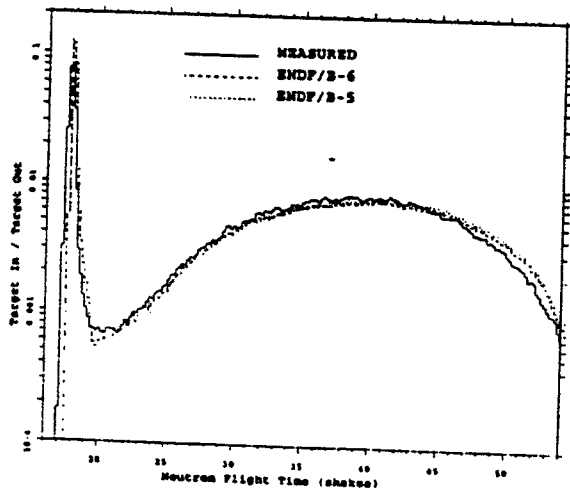


Figure 36. Normalized time-of-flight spectra for 1.5 mfp ^{235}U .

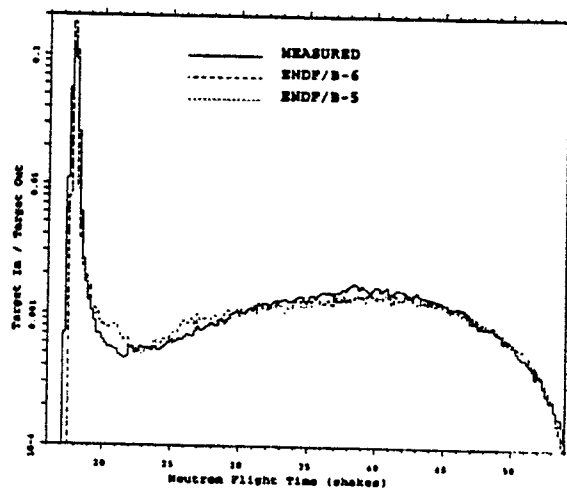


Figure 37. Normalized time-of-flight spectra for 0.8 mfp ^{238}U .

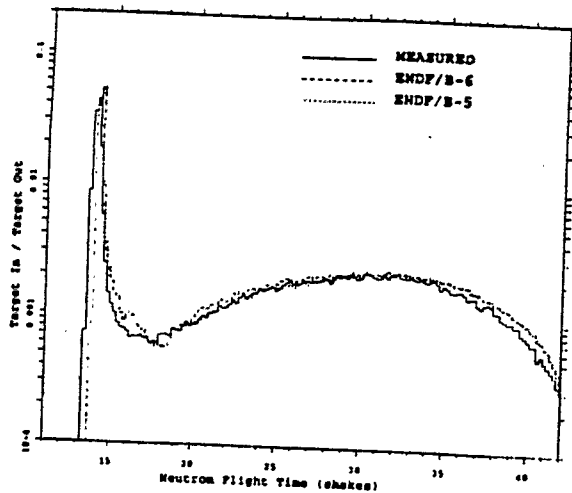


Figure 38. Normalized time-of-flight spectra for 2.8 mfp ^{238}U .

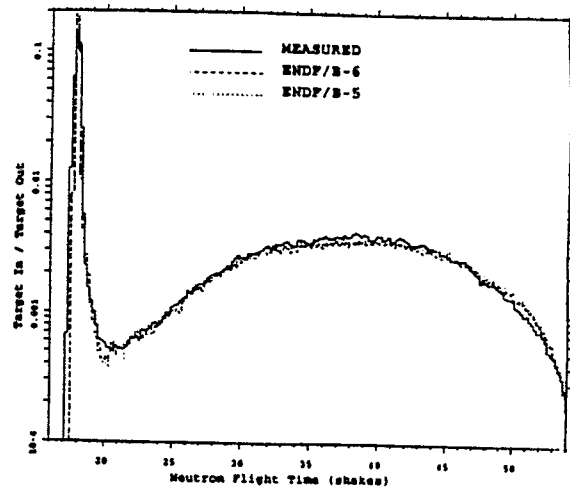


Figure 39. Normalized time-of-flight spectra for 0.7 mfp ^{239}Pu .

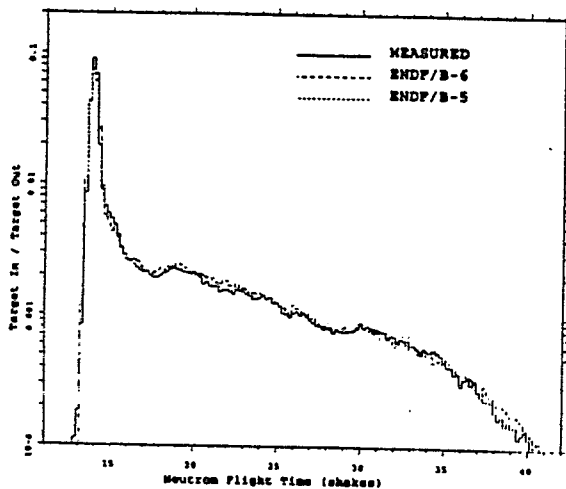


Figure 40. Normalized time-of-flight spectra for 1.1 mfp light water (H_2O).

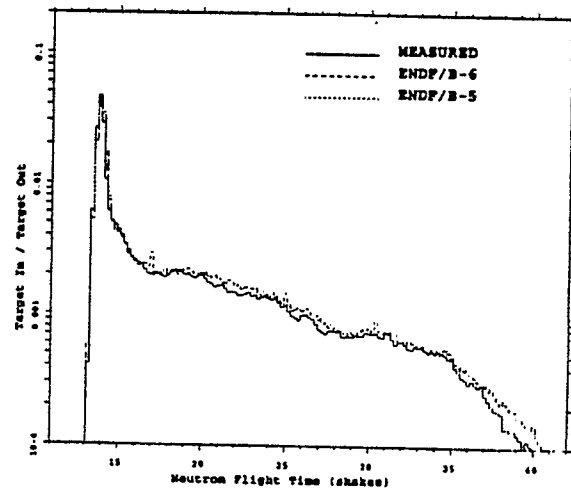


Figure 41. Normalized time-of-flight spectra for 1.9 mfp light water (H_2O).

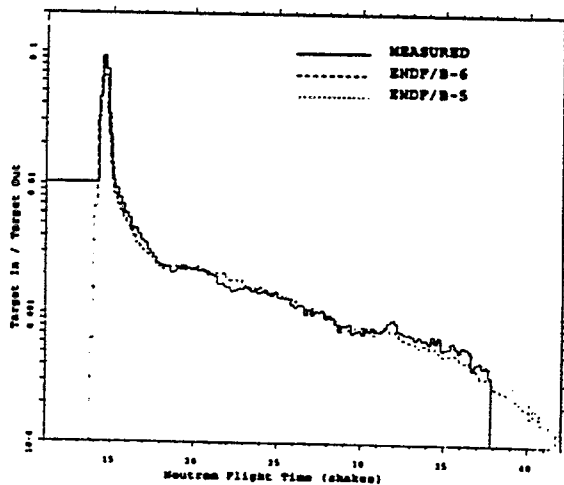


Figure 42. Normalized time-of-flight spectra for 1.2 mfp heavy water (D_2O).

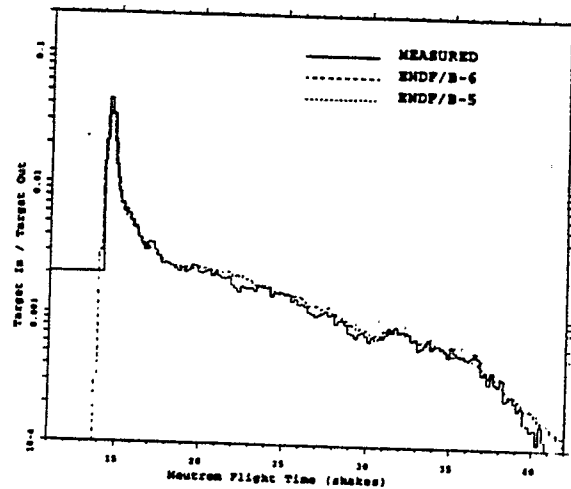


Figure 43. Normalized time-of-flight spectra for 2.1 mfp heavy water (D_2O).

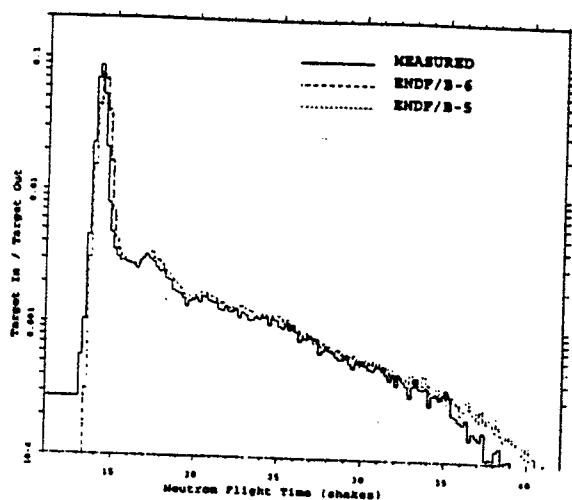


Figure 44. Normalized time-of-flight spectra for 0.8 mfp polyethylene (CH_2).

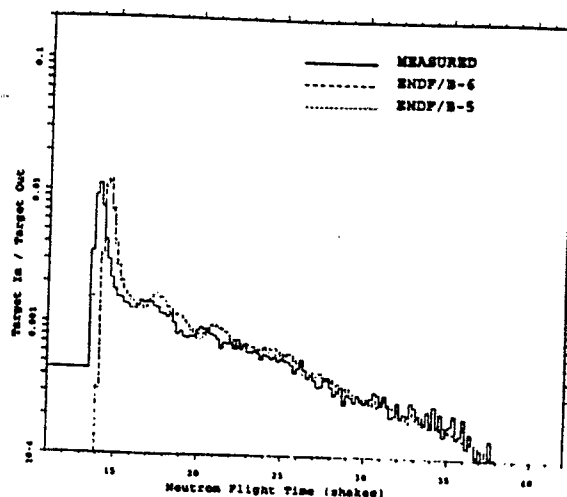


Figure 45. Normalized time-of-flight spectra for 3.5 mfp polyethylene (CH_2).

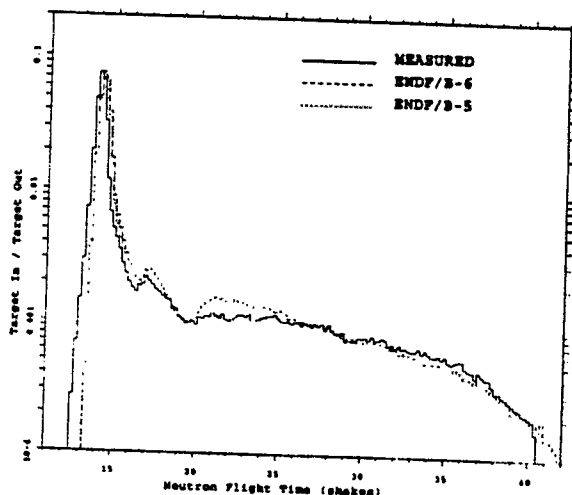


Figure 46. Normalized time-of-flight spectra for 0.9 mfp teflon (CF_2).

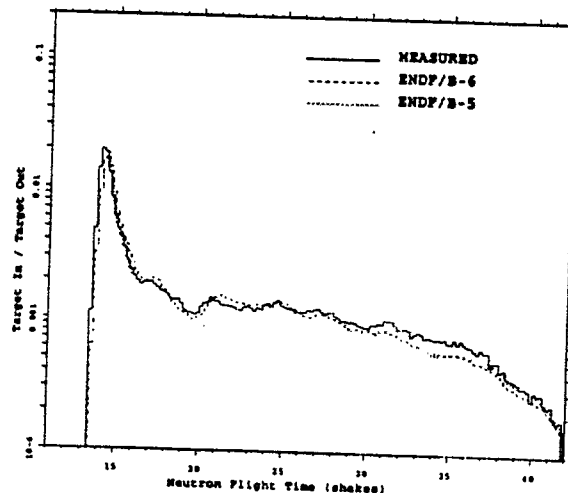


Figure 47. Normalized time-of-flight spectra for 2.9 mfp teflon (CF_2).

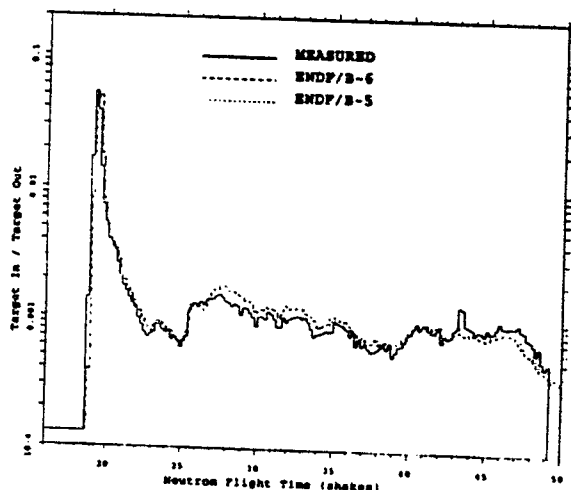


Figure 48. Normalized time-of-flight spectra for 2.0 mfp concrete.

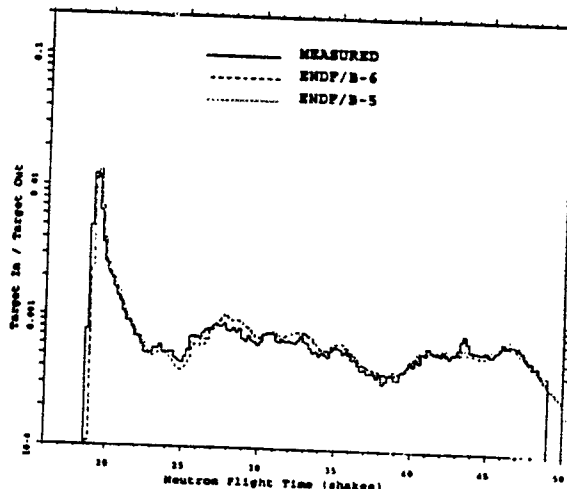


Figure 49. Normalized time-of-flight spectra for 3.8 mfp concrete.

Table 35. Results of Pulsed Sphere Benchmarks with ENDF/B-V and ENDF/B-VI.

Material	Radius (mfp)	Energy Bin (MeV)	Ratio of ENDF/B-V to Measurement	Ratio of ENDF/B-VI to Measurement
⁶ Li	0.5	2 - 3	1.00	1.04
		3 - 5	1.15	1.28
		5 - 10	0.94	1.10
		10 - 13	0.80	0.86
		13 - 16	1.02	0.98
	1.6	2 - 3	1.15	1.19
		3 - 5	1.20	1.29
		5 - 10	0.93	1.04
		10 - 13	1.01	0.92
		13 - 16	1.07	0.97
⁷ Li	0.5	2 - 3	0.84	0.88
		3 - 5	0.82	0.85
		5 - 10	0.91	0.87
		10 - 13	0.89	0.89
		13 - 16	1.01	1.01
	1.6	2 - 3	0.96	1.00
		3 - 5	0.93	0.96
		5 - 10	0.97	0.93
		10 - 13	1.08	1.08
		13 - 16	1.05	1.05
Be	0.8	2 - 3	1.01	0.87
		3 - 5	1.25	1.05
		5 - 10	1.23	1.11
		10 - 13	1.12	1.01
		13 - 16	0.96	0.99
C	0.5	2 - 3	0.92	0.65
		3 - 5	0.95	1.02
		5 - 10	1.27	1.39
		10 - 13	1.01	1.06
		13 - 16	1.02	1.04
	2.9	2 - 3	0.84	0.80
		3 - 5	0.95	1.07
		5 - 10	1.05	1.19
		10 - 13	0.95	1.03
		13 - 16	0.93	1.00
N	1.1	2 - 3	1.15	1.04
		3 - 5	1.41	1.12
		5 - 10	1.26	1.22
		10 - 13	0.82	0.94
		13 - 16	0.87	0.90

Table 35 (cont). Results of Pulsed Sphere Benchmarks with ENDF/B-V and ENDF/B-VI.

Material	Radius (mfp)	Energy Bin (MeV)	Ratio of ENDF/B-V to Measurement	Ratio of ENDF/B-VI to Measurement
N	3.1	2 - 3	1.20	1.07
		3 - 5	1.37	1.16
		5 - 10	1.18	1.17
		10 - 13	0.77	0.94
		13 - 16	0.85	0.93
O	0.7	2 - 3	1.28	0.87
		3 - 5	1.38	1.25
		5 - 10	1.28	1.41
		10 - 13	0.87	0.96
		13 - 16	0.93	0.91
Mg	0.7	2 - 3	0.84	0.83
		3 - 5	0.88	0.87
		5 - 10	1.03	1.02
		10 - 13	1.21	1.22
		13 - 16	1.15	1.16
	1.9	2 - 3	0.80	0.80
		3 - 5	0.84	0.83
		5 - 10	0.94	0.94
		10 - 13	1.26	1.26
		13 - 16	1.15	1.15
Al	0.9	2 - 3	0.96	0.96
		3 - 5	0.89	0.89
		5 - 10	1.14	1.14
		10 - 13	0.87	0.88
		13 - 16	1.17	1.17
	2.6	2 - 3	0.91	0.91
		3 - 5	0.85	0.85
		5 - 10	1.04	1.03
		10 - 13	0.88	0.88
		13 - 16	0.91	0.91
Ti	1.2	2 - 3	0.80	0.80
		3 - 5	0.62	0.61
		5 - 10	0.99	0.97
		10 - 13	0.89	0.91
		13 - 16	1.19	1.19
	3.5	2 - 3	0.75	0.74
		3 - 5	0.60	0.60
		5 - 10	0.97	0.97
		10 - 13	1.13	1.13
		13 - 16	1.35	1.35

Table 35 (cont). Results of Pulsed Sphere Benchmarks with ENDF/B-V and ENDF/B-VI.

Material	Radius (mfp)	Energy Bin (MeV)	Ratio of ENDF/B-V to Measurement	Ratio of ENDF/B-VI to Measurement
Fe	0.9	2 - 3	0.84	0.80
		3 - 5	0.88	0.96
		5 - 10	1.19	1.28
		10 - 13	0.79	0.89
		13 - 16	0.52	0.53
	4.8	2 - 3	0.87	0.91
		3 - 5	0.81	1.00
		5 - 10	0.95	1.26
		10 - 13	0.70	0.86
		13 - 16	0.63	0.67
W	0.9	2 - 3	0.79	0.78
		3 - 5	0.98	0.95
		5 - 10	1.28	1.22
		10 - 13	0.81	0.84
		13 - 16	1.07	1.07
	3.2	2 - 3	0.76	0.75
		3 - 5	0.90	0.92
		5 - 10	1.11	1.06
		10 - 13	0.68	0.68
		13 - 16	1.00	1.00
Pb	1.4	2 - 3	0.58	0.76
		3 - 5	0.69	0.93
		5 - 10	1.13	1.08
		10 - 13	1.05	1.07
		13 - 16	0.92	0.92
²³⁵ U	0.7	2 - 3	0.92	0.93
		3 - 5	0.87	0.86
		5 - 10	0.95	0.93
		10 - 13	1.18	1.03
		13 - 16	0.96	0.94
	1.5	2 - 3	1.02	0.97
		3 - 5	0.91	0.89
		5 - 10	0.93	0.91
		10 - 13	1.18	0.98
		13 - 16	0.99	0.95
²³⁸ U	0.8	2 - 3	0.95	0.92
		3 - 5	0.87	0.92
		5 - 10	1.02	1.13
		10 - 13	1.42	1.45
		13 - 16	0.94	0.95

Table 35 (cont). Results of Pulsed Sphere Benchmarks with ENDF/B-V and ENDF/B-VI.

Material	Radius (mfp)	Energy Bin (MeV)	Ratio of ENDF/B-V to Measurement	Ratio of ENDF/B-VI to Measurement
²³⁵ U	2.8	2 - 3	1.05	1.05
		3 - 5	0.97	1.02
		5 - 10	0.91	1.04
		10 - 13	1.26	1.26
		13 - 16	0.96	1.00
²³⁹ Pu	0.7	2 - 3	1.00	0.95
		3 - 5	0.95	0.90
		5 - 10	0.98	0.96
		10 - 13	0.92	0.99
		13 - 16	0.95	0.96
Light Water (H ₂ O)	1.1	2 - 3	1.07	0.96
		3 - 5	1.06	1.03
		5 - 10	1.06	1.07
		10 - 13	0.94	0.94
		13 - 16	0.94	0.93
	1.9	2 - 3	1.15	1.07
		3 - 5	1.13	1.10
		5 - 10	1.08	1.09
		10 - 13	1.00	1.01
		13 - 16	1.00	0.98
Heavy Water (D ₂ O)	1.2	2 - 3	1.22	0.97
		3 - 5	1.13	1.01
		5 - 10	1.04	1.05
		10 - 13	0.85	0.87
		13 - 16	0.86	0.85
	2.1	2 - 3	1.17	0.99
		3 - 5	1.15	1.07
		5 - 10	1.06	1.07
		10 - 13	0.95	0.95
		13 - 16	0.97	0.96
Polyethylene (CH ₂)	0.8	2 - 3	1.25	1.16
		3 - 5	1.05	1.07
		5 - 10	1.08	1.11
		10 - 13	1.04	1.06
		13 - 16	1.04	1.06
	3.5	2 - 3	0.97	0.98
		3 - 5	1.03	1.07
		5 - 10	1.11	1.16
		10 - 13	1.05	1.09
		13 - 16	1.49	1.57

Table 35 (cont). Results of Pulsed Sphere Benchmarks with ENDF/B-V and ENDF/B-VI.

Material	Radius (mfp)	Energy Bin (MeV)	Ratio of ENDF/B-V to Measurement	Ratio of ENDF/B-VI to Measurement
Teflon (CF ₂)	0.9	2 - 3	1.14	0.89
		3 - 5	1.07	1.03
		5 - 10	1.01	1.19
		10 - 13	1.15	1.31
		13 - 16	1.10	1.17
	2.9	2 - 3	0.81	0.82
		3 - 5	0.84	0.94
		5 - 10	0.80	1.02
		10 - 13	0.88	1.13
		13 - 16	0.77	0.92
Concrete	2.0	2 - 3	1.02	0.92
		3 - 5	1.10	1.13
		5 - 10	1.14	1.14
		10 - 13	1.15	1.13
		13 - 16	0.97	0.97
	3.8	2 - 3	1.08	1.01
		3 - 5	1.09	1.10
		5 - 10	1.06	1.02
		10 - 13	1.12	1.07
		13 - 16	0.89	0.89

The ENDF/B-VI results for Be produce much better agreement with the measurements than do those from ENDF/B-V, although both underestimate the flux at energies below 2.5 MeV. The ENDF/B-VI results for C, however, are not as good as those from ENDF/B-V, although both underestimate the flux at the lowest energies. The ENDF/B-VI results for N produce improvement similar to that seen for Be, although both ENDF/B-VI and ENDF/B-V overestimate the flux at lower energies for the larger sphere. The results for O still show poor agreement with measurement, although ENDF/B-VI shows improvement at the lower energies. The ENDF/B-VI results for Pb indicate a significant improvement over the corresponding ENDF/B-V results. (ENDF/B-VI has an evaluation for each isotope of Pb, while ENDF/B-V contained only a single evaluation for the element.) However, the flux for Pb still is somewhat underestimated at lower energies. The results shown here for Fe are not conclusive. However, other studies⁷⁴ have indicated that the ENDF/B-VI evaluation is an improvement over ENDF/B-V.

The results for Al, Mg, Ti, and W are equivalent because the ENDF/B-V evaluations for those elements have been retained through ENDF/B-VI.2. Mg shows reasonable agreement for the smaller spheres, but the agreement is poor for the larger sphere. The Al results indicate reasonable agreement over the entire energy range, while the Ti results show very poor agreement. The W results indicate a significant underestimate of the flux at energies below 3.7 MeV.

Both ENDF/B-V and ENDF/B-VI produce good agreement with the measured results for the fissionable nuclides. In particular, ENDF/B-VI produces improved results for ²³⁵U in the energy range between 7.6 and 13 MeV. The results for ²³⁸U show an overestimate of the flux from 10 to 13 MeV. In addition, ENDF/B-VI produces a slight increase in the

flux over the energy range from 4 to 6 MeV relative to ENDF/B-V. The results for ^{239}Pu show no significant differences between ENDF/B-V and ENDF/B-VI.

There is good agreement for the light- and heavy-water spheres and the polyethylene spheres for both data libraries, although the ENDF/B-VI data do show some improvement over ENDF/B-V. There also is improvement in the teflon spheres for ENDF/B-VI, particularly for the thicker sphere. The concrete spheres were composed primarily of O, H, and Si, and they show good agreement for both sets of evaluations.

CONCLUSIONS AND RECOMMENDATIONS

ENDF/B-VI produces good to excellent agreement with most of the benchmark measurements studied herein. It also produces results that are very similar to those from ENDF/B-V for a majority of them. However, it produces dramatically better results for a few cases and slightly worse results for a few others.

Improvements in ENDF/B-VI

The most obvious success for ENDF/B-VI is the dramatic improvement in the agreement with the benchmark values of k_{eff} for plutonium nitrate solutions, an area in which previous versions of ENDF/B had not performed well. In addition, ENDF/B-VI improves the agreement with benchmark values of k_{eff} for some other critical configurations relative to ENDF/B-V, including the Jemima experiments and SHEBA-II.

For most of the reactor lattices and solutions examined in this study, ENDF/B-VI.3 produces negligible to marginal changes in reactivity relative to ENDF/B-VI.2. However, the results for NB-5 and the sphere of uranyl fluoride in heavy water demonstrate that ENDF/B-VI.3 decreases the reactivity significantly for lattices and solutions with harder spectra.

ENDF/B-VI produces significantly better agreement than ENDF/B-V with time-of-flight measurements for several materials, including Be, N, Pb, ^{235}U , and heavy water. The improvement for Be and N extends throughout the energy range between 2 and 16 MeV. However, the improvement for Pb and heavy water occurs primarily in the range between 2 and 5 MeV, while the improvement for ^{235}U occurs primarily in the range between 7.6 and 13 MeV.

Deficiencies in ENDF/B-VI

Although ENDF/B-VI agrees as well as or better than ENDF/B-V with most of the benchmarks, there are a few for which it produces marginally worse agreement. In particular, it underestimates k_{eff} by a larger margin than ENDF/B-V for Godiva, the B&W lattices, and the solutions of HEU uranyl nitrate. In general, ENDF/B-VI appears to increase neutron leakage relative to ENDF/B-V. Consequently it tends to produce slightly better agreement than ENDF/B-V for those benchmarks where ENDF/B-V overpredicts k_{eff} but to produce slightly worse agreement for those where ENDF/B-V underpredicts k_{eff} . (The notable exception to this generalization is the sphere of uranyl fluoride in heavy water, which has a spectrum that is significantly harder than those of the other solutions.)

ENDF/B-VI produces slightly worse agreement with the time-of-flight benchmarks for C than ENDF/B-V does. The deterioration occurs throughout most of the energy range between 2 and 16 MeV, but it is particularly noticeable at the lowest energies.

Although the ENDF/B-VI and ENDF/B-V evaluations for O produce significantly different results for the time-of-flight benchmarks, neither of them produce good agreement.

ENDF/B-VI produces reasonable agreement above 10 MeV, but the agreement with measurement deteriorates at lower energies.

Additional deficiencies in ENDF/B-VI are carryovers from ENDF/B-V. In particular, the cross sections for ^{233}U produce a significant underestimate of k_{eff} for the Jemima-233 benchmark, and Ti shows poor agreement with the time-of-flight benchmarks. In addition, the tendency to overestimate leakage for bare spheres of uranium is common to both ENDF/B-V and ENDF/B-VI.

Other Observations

There are some other differences between results from ENDF/B-VI and ENDF/B-V, but at this point it is not clear whether those differences represent improvements. Specifically, ENDF/B-VI produces a more pronounced variation in reactivity with enrichment for LEU lattices than ENDF/B-V does. Furthermore, relative to ENDF/B-V, ^{16}O produces small but significant reactivity differences for many of the cases with thermal spectra. This behavior improves the agreement with plutonium solution benchmarks, but it worsens the agreement for spheres of uranium nitrate.

Recommendations

Further revisions to the ENDF/B-VI evaluation for ^{235}U already are under way. However, based on the results obtained herein, there are other areas that should be improved as well.

Spheres of HEU and ^{233}U both exhibit significant reactivity swings between bare and reflected configurations. This behavior suggests that the current effort to revise the evaluation for ^{235}U should be extended to include the total cross section at high energies (~ 1 MeV). In addition, the cross sections for ^{233}U at high energies need to be revised to improve agreement with the Jezebel-233 benchmark and to reduce the reactivity swing between bare and reflected configurations.

The ENDF/B-V evaluation for Ti was carried forward to ENDF/B-VI, but the time-of-flight benchmarks clearly indicate that it needs to be revised.

The evaluation for ^{16}O needs to be revisited as well. As the comparison with time-of-flight benchmarks indicates, the ENDF/B-VI cross sections for ^{16}O are deficient between 2 and 10 MeV. In addition, the ENDF/B-VI evaluation for ^{16}O tends to produce more leakage in critical configurations than its predecessor did, and it also reduces reactivity slightly in cases with thermal spectra.

ACKNOWLEDGMENTS

We would like to thank a number of our colleagues at LANL for their contributions, without which much of this study could not have been performed. Robert E. MacFarlane prepared the unthinned ENDF/B-VI libraries for MCNP. Joseph L. Sapir, Raphael J. LaBauve, and Roger W. Brewer provided us with benchmark specifications for several of the critical experiments prior to the formal publication of those specifications. Denise B. Pelowitz gave us an MCNP input deck for the (very) complicated model of the MHTGR lattice. Guy P. Estes, Ronald C. Brockhoff, and J. David Court provided information on the previous implementation of the LLNL pulsed-sphere benchmarks, and Robert C. Little provided many helpful discussions on the results.

REFERENCES

1. Judith F. Briesmeister, ed., "MCNP—a general Monte Carlo n-particle transport code, version 4a," LA-12625-M, Los Alamos National Laboratory (November 1993).
2. R. Kinsey, "ENDF-201: ENDF/B summary documentation," BNL-NCS-17541, Brookhaven National Laboratory (1979).
3. B. A. Magurno and P. G. Young, "ENDF-201 supplement 1: ENDF/B-V.2 summary documentation," BNL-NCS-17541, Brookhaven National Laboratory (1985).
4. See S. Pearlstein, "Nuclear data for nuclear reactor analyses — an overview," *Prog. Nucl. En.*, 13:75 (1984) and subsequent articles in that volume.
5. G. Breit and E. Wigner, "Capture of Slow Neutrons," *Phys. Rev.* 49:519 (1936); see also, George I. Bell and Samuel Glasstone, **Nuclear Reactor Theory**, pp. 391-398, Van Nostrand Reinhold Company (1970).
6. P. F. Rose and C. L. Dunford, "ENDF-102: data formats and procedures for the evaluated nuclear data file ENDF-6," BNL-NCS-44945, Brookhaven National Laboratory (1991).
7. F. T. Adler and D. B. Adler, "Interpretations of neutron cross sections of the fissionable materials for the resolved resonance region," P. B. Hemmig, Ed., *Proc. Conf. on Neutron Cross Section Technology*, CONF-660303, Vol. II, pp. 873-894 (1967).
8. R. E. MacFarlane, "Energy balance of ENDF/B-V," *Trans. Am. Nucl. Soc.* 33:681 (1979).
9. C. R. Weisbin, R. D. McKnight, J. Hardy, Jr., R. W. Roussin, R. E. Schenter, and B. A. Magurno, "Benchmark Data Testing of ENDF/B-V," BNL-NCS-31531, Brookhaven National Laboratory (1982).
10. P. F. Rose, "ENDF-201: ENDF/B-VI summary documentation," BNL-NCS-17541, Brookhaven National Laboratory (1991).
11. A. D. Carlson, W. P. Poenitz, G. M. Hale, R. W. Peele, D. C. Dodder, C. Y. Fu, and W. Mannhart, "The ENDF/B-VI neutron measurement standards," NISTIR 5177 (ENDF-351), National Institute of Standards and Technology (1993).
12. V. McLane, "ENDF-201 supplement: ENDF/B-VI summary documentation," BNL-NCS-17541, supplement 1, Brookhaven National Laboratory (1996).
13. S. T. Perkins, E. F. Plechaty, and R. J. Howerton, "A reevaluation of the $^9\text{Be}(n,2n)$ reaction and its effect on neutron multiplication in fusion blanket applications," *Nucl. Sci. Eng.* 90:83 (1985).
14. For example, see D. M. Hetrick, C. Y. Fu, and D. C. Larson, "Calculated neutron-induced cross sections for $^{58,60}\text{Ni}$ from 1 to 20 MeV and comparisons with experiments," ORNL/TM-10219, Oak Ridge National Laboratory (1987).
15. C. M. Perey, F. G. Perey, J. A. Harvey, N. W. Hill, N. M. Larson, and R. L. Macklin, " $^{58}\text{Ni} + n$ transmission, differential elastic scattering, and capture measurements and analysis from 5 to 813 keV," ORNL/TM-10841, Oak Ridge National Laboratory (1988).
16. For example, see H. Derrien, G. De Saussure, R. B. Perez, N. M. Larson, and R. L. Macklin, "R-matrix analysis of the ^{239}Pu cross sections up to 1 kev," ORNL/TM-10098, Oak Ridge National Laboratory (1986).
17. C. W. Reich and M. S. Moore, "Multilevel formula for the fission process," *Phys. Rev.*, 111:929 (1968).
18. T. R. England and B. F. Rider, "Evaluation and compilation of fission product yields — 1993," LA-UR-94-3106 (ENDF-349), Los Alamos National Laboratory (1994).
19. T. R. England, J. Katakura, F. M. Mann, C. W. Reich, R. E. Schenter, and W. B. Wilson, "Decay data evaluation for ENDF/B-VI," *Proc. Sym. on Nuclear Data Evaluation Methodology*, Brookhaven National Laboratory, Upton, NY, 12-16 October 1992, p. 611.
20. S. C. Frankle, "A revised table 1 for appendix g of the MCNP4A manual," XTM:96-146, Los Alamos National Laboratory (1996).
21. "Cross section evaluation working group benchmark specifications," BNL-19302 (ENDF-202), Brookhaven National Laboratory (November 1974).
22. "International handbook of evaluated criticality safety benchmark experiments," NEA/NSC/DOC(95)03, OECD Nuclear Energy Agency (April 1995).
23. G. E. Hansen and H. C. Paxton, "Re-evaluated critical specifications of some Los Alamos fast-neutron systems," LA-4208, Los Alamos Scientific Laboratory (June 1969).
24. R. E. Peterson, "Lady Godiva: an unreflected uranium-235 critical assembly," LA-1614, Los Alamos Scientific Laboratory (September 1953).
25. V. Josephson, "Critical-mass measurements on oralloys in tuballoy and WC tampers," LA-1114, Los Alamos Scientific Laboratory (May 1950).

26. H. C. Paxton, "Los Alamos Critical-Mass Data," LA-3067-MS, Rev., Los Alamos Scientific Laboratory (December 1975).
27. H. C. Paxton, "Bare critical assemblies of oralloy at intermediate concentrations of ^{235}U ," LA-1671, Los Alamos Scientific Laboratory (July 1954).
28. Cleo C. Byers, Jerry J. Koelling, Gordon E. Hansen, David R. Smith, and Howard R. Dyer, "Critical measurements of a water-reflected enriched uranium sphere," *Trans. Am. Nucl. Soc.* 27:412 (1977).
29. R. G. Taylor, "Fabrication and isotopic data for the water reflected U(97.67) metal sphere critical experiment," Y/DD-622, Oak Ridge Y-12 Plant (November 1993).
30. J. C. Hoogterp, "Critical masses of oralloy lattices immersed in water," LA-2026, Los Alamos Scientific Laboratory (March 1957).
31. M. N. Baldwin and M. E. Stern, "Physics verification program, part III, task 4, summary report," BAW-3647-20, Babcock & Wilcox (March 1971).
32. D. J. Diamond, R. D. Mosteller, and J. C. Gehin, "Ad hoc committee on reactor physics benchmarks," *Trans. Am. Nucl. Soc.*, 74:285 (1996).
33. Russell D. Mosteller, "Benchmarking of MCNP against B&W LRC core XI critical experiments," *Trans. Am. Nucl. Soc.*, 73:444 (1995).
34. F. Rahnema and H. N. M. Gheorghiu, "ENDF/B-VI benchmark calculations for the Doppler coefficient of reactivity," *Ann. Nucl. Energy*, 23:1011 (1996).
35. R. Gwin and D. W. Magnuson, "Eta of ^{233}U and ^{235}U for critical experiments," *Nucl. Sci. Eng.* 12:364 (1962).
36. Alan Staub, D. R. Harris, and Mark Goldsmith, "Analysis of a set of critical homogeneous U-H₂O spheres," *Nucl. Sci. Eng.* 34:263 (1968).
37. Michelle Pitts, Farzad Rahnema, T. G. Williamson, and Fitz Trumble, "Benchmark description for unreflected 174-l spheres containing uranyl nitrate," *Trans. Am. Nucl. Soc.*, 74:227 (1996).
38. Richard N. Olcott, "Homogeneous heavy water moderated critical assemblies. part 1. experimental," *Nucl. Sci. Eng.* 1:327 (1956).
39. Kenneth B. Butterfield, "The SHEBA experiment," *Trans. Am. Nucl. Soc.* 70:199 (1994).
40. R. J. LaBauve and Joseph L. Sapir, "SHEBA-II as a criticality safety benchmark," *Proceedings of the Fifth International Conference on Nuclear Criticality Safety* (September 1995).
41. G. A. Jarvis, G. A. Linenberger, D. D. Orndoff, and H. C. Paxton, "Two plutonium-metal critical assemblies," *Nucl. Sci. Eng.* 8:525 (1960).
42. L. B. Engle, G. E. Hansen, and H. C. Paxton, "Reactivity contributions of various materials in Topsy, Godiva, and Jezebel," *Nucl. Sci. Eng.* 8:543 (1960).
43. David R. Smith and William U. Geer, "Critical mass of a water-reflected plutonium sphere," *Nucl. Appl. Technol.* 7:405 (1969).
44. R. I. Smith and G. J. Konzek, "Clean critical experiment benchmarks for plutonium recycle in LWR's," NP-196, Vol. I, Electric Power Research Institute (April 1976).
45. R. Sher and S. Fiarman, "Analysis of some uranium oxide and mixed-oxide lattice measurements," NP-691, Electric Power Research Institute (February 1978).
46. R. C. Lloyd, C. R. Richey, E. D. Clayton, and D. R. Skeen, "Criticality studies with plutonium solutions," *Nucl. Sci. Eng.* 25:165 (1966).
47. C. R. Richey, "Theoretical analyses of homogeneous plutonium critical experiments," *Nucl. Sci. Eng.* 31:32 (1968).
48. R. Q. Wright, Oak Ridge National Laboratory, private communication (May 1995).
49. M. L. Williams, R. Q. Wright, J. Barhen, W. Rothenstein, and B. Toney, "Benchmarking of epithermal methods in the lattice physics code EPRI-CELL," in: *Proceedings: Thermal Reactor Benchmark Calculations, Techniques, Results, and Applications*, P. F. Rose, ed., NP-2855, Electric Power Research Institute (February 1983).
50. M. L. Williams, R. Q. Wright, and J. Barhen, "Improvements in EPRI-CELL methods and benchmarking of the ENDF/B-V cross-section library," NP-2416, Electric Power Research Institute (June 1982).
51. R. D. Mosteller, L. D. Eisenhart, R. C. Little, W. J. Eich, and J. Chao, "Benchmark calculations for the Doppler coefficient of reactivity," *Nucl. Sci. Eng.*, 107:265 (March 1991).
52. J. R. Brown, *et al.*, "Kinetic and buckling measurements of lattices of slightly enriched uranium or UO₂ rods in light water," WAPD-176, Bettis Atomic Power Laboratory (January 1958).
53. A. R. Boynton, Q. L. Baird, K. E. Plumlee, W. C. Redman, W. R. Robinson, and G. S. Stanford, "High conversion critical experiments," ANL-7203, Argonne National Laboratory (January 1967).

54. R. D. Mosteller, J. T. Holly, and L. A. Mott, "Benchmark calculations for the Doppler coefficient of reactivity in mixed-oxide fuel," *Proceedings of the International Topical Meeting on Advances in Mathematics, Computations, and Reactor Physics*, CONF-910414 (April 1991).
55. N. H. Larsen, "Core design and operating data for cycles 1 and 2 of peach bottom 2," NP-563, Electric Power Research Institute (June 1978).
56. R. D. Mosteller and F. J. Rahn, "Monte Carlo calculations for recriticality during the reflood phase of a severe accident in a boiling water reactor," *Nucl. Technol.*, 110:168 (1995).
57. "Russian RBMK reactor design information," PNL-8937, Pacific Northwest Laboratory (November 1993).
58. Denise B. Pelowitz, Joseph L. Sapir, and Janet E. Wing, "Analysis of the NP-MHTGR concept: a comparison of reactor physics methods," *Proceedings of the 1992 Topical Meeting on Advances in Reactor Physics* (March 1992).
59. J. Griffiths, "WIMS-AECL users manual," RC-1176, COG-94-52, Chalk River Laboratories (March 1994).
60. R. T. Perry, R. D. Mosteller, J. R. Streetman, J. L. Sapir, and R. J. J. Stamm'ler, "Preliminary benchmarking of the HELIOS code for hexagonal lattice reactors," *Trans. Am. Nucl. Soc.*, 66:513 (1992).
61. C. R. Lubitz, "A modification to ENDF/B-VI ^{235}U to increase epithermal alpha and K_1 ," *Proceedings of the International Conference on Nuclear Data for Science and Technology*, CONF-940507 (May 1994).
62. A. C. Kahler, "Homogeneous critical Monte Carlo eigenvalue calculations with revised ENDF/B-VI data sets," *Trans. Am. Nucl. Soc.*, 72:384 (1995).
63. M. L. Williams, R. Q. Wright, and M. Asgari, "ENDF/B-VI performance for thermal reactor analysis," *Trans. Am. Nucl. Soc.*, 73:420 (1995).
64. E. Goldberg, L. F. Hansen, T. T. Komoto, B. A. Pohl, R. J. Howerton, R. E. Dye, E. F. Plechaty, and W. E. Warren, "Neutron and gamma-ray spectra from a variety of materials bombarded with 14-MeV neutrons," *Nucl. Sci. Eng.* 105:319 (1990).
65. L. F. Hansen, *et al.*, "Updated summary of measurements and calculations of neutron and gamma-ray emission spectra from spheres pulsed with 14-MeV neutrons," UCID-19604, Rev. 1, Lawrence Livermore National Laboratory (1989).
66. C. Wong, *et al.*, "Livermore pulsed sphere program: program summary through July 1971," UCRL-51144, Rev. 1, Lawrence Livermore National Laboratory (1972).
67. W. M. Webster and P. S. Brown, "Low energy time-of-flight spectra from spheres pulsed by 14-MeV neutrons," UCID-17223, Lawrence Livermore National Laboratory (1976).
68. W. M. Webster, *et al.*, "Measurements of the neutron emission spectra from spheres of N, O, W, ^{235}U , ^{238}U , and ^{239}Pu , pulsed by 14-MeV neutrons," UCID-17332, Lawrence Livermore National Laboratory (1976).
69. E. F. Plechaty and R. J. Howerton, "Calculational model for LLL pulsed spheres (CSEWG shielding benchmark collection no. STD 10)," UCID-16372, Lawrence Livermore National Laboratory (1973).
70. G. P. Estes, "Pulsed sphere calculations with ENDF/B-V cross sections (for transmittal to CSEWG)," Los Alamos National Laboratory memoranda (October 24, 1979 and May 9, 1980).
71. Daniel J. Whalen, David A. Cardon, Jennifer L. Uhle, and John S. Hendricks, "MCNP: neutron benchmark problems," LA-12212, Los Alamos National Laboratory (1991).
72. John D. Court, Ronald C. Brockhoff, and John S. Hendricks, "Lawrence livermore pulsed sphere benchmark analysis of MCNP ENDF/B-VI," LA-12885, Los Alamos National Laboratory (1994).
73. S. C. Frankle, "Revised LLNL pulsed sphere benchmarks for MCNP," to be published by Los Alamos National Laboratory.
74. John D. Court and John S. Hendricks, "Benchmark analysis of MCNP ENDF/B-VI iron," LA-12884, Los Alamos National Laboratory (1994).

APPENDIX A: IDENTIFIERS FOR CSEWG AND ICSBEP BENCHMARKS

Table A-1. CSEWG and ICSBEP Identifiers for Benchmark Critical Experiments.

Case Title	Benchmark Identifier	
	CSEWG	ICSBEP
Godiva	Fast reactor #5	HEU-MET-FAST-001
Topsy sphere		HEU-MET-FAST-002
FLATTOP-25	Fast reactor #22	HEU-MET-FAST-026 ^a
Jemima pairs		IEU-MET-FAST-001
Jemima triplets		IEU-MET-FAST-001
HEU sphere in water		HEU-MET-FAST-004
HEU cube in water		HEU-MET-FAST-006
Jezebel-233	Fast reactor #19	U233-MET-FAST-001
FLATTOP-23	Fast reactor #24	U233-MET-FAST-005
B&W core XI, loading 1		LEU-COMP-THERM-008
B&W core XI, loading 2		LEU-COMP-THERM-008
B&W core XI, loading 8		LEU-COMP-THERM-008
ORNL-1	Thermal reactor #1	HEU-SOL-THERM-013
ORNL-2	Thermal reactor #2	HEU-SOL-THERM-013
ORNL-3	Thermal reactor #3	HEU-SOL-THERM-013
ORNL-4	Thermal reactor #4	HEU-SOL-THERM-013
ORNL-10	Thermal reactor #5	
SHEBA-II		LEU-SOL-THERM-001 ^a
Uranyl fluoride in D ₂ O		HEU-SOL-THERM-004
ORNL-5		U233-SOL-THERM-001
ORNL-6		U233-SOL-THERM-001
ORNL-7		U233-SOL-THERM-001
ORNL-8		U233-SOL-THERM-001
ORNL-9		U233-SOL-THERM-001
Jezebel	Fast reactor #1	PU-MET-FAST-001
Jezebel-240	Fast reactor #21	PU-MET-FAST-002
FLATTOP-Pu	Fast reactor #23	PU-MET-FAST-006 ^a
Pu sphere in water		PU-MET-FAST-011
PNL-30	Thermal reactor #31	MIX-COMP-THERM-002 ^a
PNL-31	Thermal reactor #32	MIX-COMP-THERM-002 ^a
PNL-32	Thermal reactor #33	MIX-COMP-THERM-002 ^a
PNL-33	Thermal reactor #34	MIX-COMP-THERM-002 ^a
PNL-34	Thermal reactor #35	MIX-COMP-THERM-002 ^a
PNL-35	Thermal reactor #36	MIX-COMP-THERM-002 ^a
PNL-1	Thermal reactor #13	
PNL-2	Thermal reactor #14	
PNL-3	Thermal reactor #15	PU-SOL-THERM-011
PNL-4	Thermal reactor #16	PU-SOL-THERM-011
PNL-5	Thermal reactor #17	PU-SOL-THERM-011
Pu nitrate sphere		PU-SOL-THERM-004
Pu nitrate sphere, high Pu		PU-SOL-THERM-004
Pu nitrate sphere, low ²⁴⁰ Pu		PU-SOL-THERM-004

^a Specifications have not yet been formally approved